Remote Sensing of Poplar Phenophase and Leaf Miner Attack in Urban Forests

Isidora Simović *, Branko Šikoparija , Marko Panić , Mirjana Radulović and Predrag Lugonja

BioSense Institute—Research Institute for Information Technologies in Biosystems, University of Novi Sad, 21000 Novi Sad, Serbia
* Correspondence: isidora.simovic@biosense.rs

Abstract: Remote sensing of phenology is adopted as the practice in greenery monitoring. Now research is turned towards the fusion of data from various sensors to fill in the gap in time series and allow monitoring of pests and disturbances. Poplar species were monitored for the determination of the best approach for detecting phenology and disturbances. With the adjustments that include a choice of indices, wavelengths, and a setup, a multispectral camera may be used to calibrate satellite images. The image processing pipeline included different denoising and interpolation methods. The correlation of the changes in a signal of top and lateral imaging proved that the contribution of the whole canopy is reflected in satellite images. Normalized difference vegetation index (NDVI) and normalized difference red edge index (NDRE) successfully distinguished among phenophases and detected leaf miner presence, unlike enhanced vegetation index (EVI). Changes in the indices were registered before, during, and after the development of the disease. NDRE is the most sensitive as it distinguished among the different intensities of damage caused by pests but it was not able to forecast its occurrence. An efficient and accurate system for detection and monitoring of phenology enables the improvement of the phenological models' quality and creates the basis for a forecast that allows planning in various disciplines.

Keywords: phenology; Sentinel-2; multispectral imaging; data fusion; *Fenusella hortulana* (Klug; 1818); *Populus* sp.

1. Introduction

Satellite remote sensing is an effective and unbiased tool for monitoring of vegetation phenology from local to global scales [1]. Researchers further say that these methods would simplify forest management and evaluation of ecosystem processes [2]. Remote sensing techniques are appreciated for their spatial coverage as well as logistics, and continuity, consistency, and objectivity of the results [3].

Insect defoliation has been the major cause of disturbance in many forested ecosystems [4]. Not only do defoliators cause a lot of damage themselves, but the defoliators frequently increase susceptibility to secondary host infection [5] that is further detrimental for the forest ecosystems. Therefore, spectral signature was used for the detection, identification, and classification of different types of damage on stands' crowns caused by insects, diseases, or other factors [6]. Some of the advantages of remote sensing techniques are that the health of forest vegetation can be checked beyond our own eyes and can be assessed at different scales and within constant time periods [7]. Although detecting and mapping forest defoliators prove to be difficult due to multiple causes, finer resolution could help overcome part of the problem. The variety of currently available sensors allows multiscale approaches, although, in the studies of insect defoliation, the most used ones are Landsat, MODIS, and SPOT [8–10].

Urban and periurban forest monitoring is defined as detailed information on forest structure and the deliverance of relevant, long-term data sets [11]. On one hand, the

distribution of trees in an urban forest is complex and broken, and the details provided by low-resolution remote sensing images are limited. On the other hand, urban forests' health status is of utter importance as they provide environmental benefits and maintain a social balance in cities [12,13]. For these reasons, proactive management practices and a focused novel monitoring methodology are needed to protect urban forests against the threats posed by insect pests [14]. Disturbances in forest ecosystems could be cost-effectively monitored in large areas using satellite-derived spatio-temporal time series, to predict population build-ups and prevent harmful consequences to forest ecosystems. Early warning is crucial for sound forest management, and even more so for forest health [15,16]. It is important not only for the protection of natural resources and public health but also for the economy worldwide [17] as monitoring plants' physiology and phenophases is a demanding and time-consuming process that uses a lot of resources.

Although remote sensing methods can be used for big areas [18] they often do not have sufficient temporal and spatial precision [19] which limits application in urban forest management and phenology monitoring at the regional scale [20,21]. Inability to penetrate below the top layer of tree crowns limits using satellite imaging for representative monitoring in phenology research and plant protection. With the increased resolution coming with the launching of Sentinel-2, we gain the opportunity to explore the importance of multilayer phenology monitoring as a rule of thumb and justification for using satellite imaging for phenology research since we only see the top layer of the crowns, as the process may differ among upper, middle, and lower parts of the tree [22]. The validation of deriving phenology from satellite data was previously examined in the example of Turin where researchers found that the green area of the city can be overestimated by as much as 50% [23]. Analyzing 3 years of data, the same authors found that less than 30% of urban green areas had the length of season (LOS) around the mean values while other parts of the greenery had prolonged or shortened LOS. These data show the importance of the temporal resolution of remote sensing imaging. Temporal resolution is also very important considering that phenological changes (both of plants and their pests) occur rapidly and cloud cover contamination issues of the optical satellite observations further reduce the number of images available to adequately detect phenological events [1,24,25]. The effects may be significant when cloud-free imagery is not available at a specific phenological stage (e.g., peak greenness) or during a key transition stage in the vegetation growth trajectory such as the start or the end of season [26]. Several studies showed that a denser time series improves the detectability of defoliation in broadleaved trees because most broadleaved trees are able to resprout in the same year as the disturbance [27–29]. One of the tasks in this regard is to improve reference data for assessing insect disturbances [30] and we believe that exploring the relation between classical methods of monitoring (visually, with RGB camera, etc.) and remote methods (UAV, satellites, etc.) is the key element for developing remote sensing methods for pest infestation monitoring in urban forests.

Hyperspectral imaging could provide the opportunity to fill in the gaps in the satellite observations and operationalize near-real-time monitoring of insect disturbances by satellites but these data to date have not been used in the context of broadleaved nor coniferous defoliators [30]. Senf et al. [30] suggest separating insect disturbances from other agents as one of the most challenging tasks in using remote sensing data for monitoring defoliators. They found that the spatial and temporal resolutions were of utter importance for distinguishing between insects and other agents that cause changes in vegetation indices and suggest taking into consideration the intra-annual timing of a disturbance. Other authors [31] cite the size and the shape of disturbances as another factor that influences the possibility to separate defoliators. Therefore, some authors suggest using fusion from various sensors [32] or improving temporal resolution for the determination of the source of disturbances [33]. The main contribution of using the hyperspectral camera for disturbances in urban forests in our setup is the fusion with satellite data for the creation of time series with a better temporal resolution. It provides the timeline with more detailed spectral information, thus improving the quality of the data. Damage caused by insects cannot

always be monitored by traditional ground surveys due to various symptoms that are not always visible at an early stage of the disease. These subtle changes are rather identified by high-resolution hyperspectral imaging of the canopies where both changes in spectra and the texture appear [34]. Other researchers also found that hyperspectral cameras have great potential in detecting insect disturbances [35] but others highlighted that the best results are reaped when fusing spectral information from hyperspectral cameras with spatial information from satellite data [36]. Therefore, the aim of this study is to determine the best vegetation indices used for the recognition of defoliation as well as the type and position of the sensors. We will focus on the detection of poplar phenophases and leaf miner *Fenusella hortulana* (Klug, 1818) infestation by using proximal and remote sensing techniques. Accordingly, we will establish the relationship between the ground-observed physiology-based phenology at the individual plant level and the satellite-derived canopy phenology at the pixel level with the aid of multiple-source and multiple-scale observations using a variety of vegetation indices.

Serbia is not covered by phenology network monitoring and therefore lacks information in this field. This work is the first step toward creating the opportunity to remotely observe phenology. Thus, we started locally, collecting ground observation data and developing proper methodology in using various sensors available at different sites. This data set is complementary to worldwide networks and information coming from Copernicus and other open services and will allow the inspection of the accuracy and precision of such tools in this area.

2. Materials and Methods

2.1. Research Subject and Study Area

The study was conducted in Novi Sad (45.24774, 19.85458), a city situated in the Pannonian part of Serbia at 80–86 m a.s.l. Novi Sad is situated on the banks of the Danube River and the Danube–Tisa–Danube Canal. South of the Danube are the slopes (90–200 m a.s.l.) of low-lying Fruška Gora Mountain. It is characterized by a continental moderate climate with the coldest month being January (T_{mean} = 0.2 °C), the warmest month being July (T_{mean} = 21.9 °C), and the annual T_{mean} of 11.4 °C during the climatological standard normal period (1981–2010) provided by the Republic Hydrometeorological Service of Serbia. In the same period, the mean annual precipitation was about 647 mm. The lowest mean monthly relative humidity is in May (RH_{mean} = 66%), the highest is in December (RH_{mean} = 86%), and the annual RH_{mean} was about 74% [37].

During 3 successive years starting from 2018, from February–December we monitored phenophases of *Populus x canadensis* Moench (Canadian poplar) and *Populus nigra* L. (black poplar) growing in the urban forest located in a university campus in Novi Sad, Serbia (Figure 1).

In 2016, poplar miner *Fenusella hortulana* (Klug, 1818) was first recorded in Serbia and was reported to cause major damage to poplar trees in the urban area of Novi Sad [38]. Therefore, apart from recording the phenophases, we detected and assessed the presence of this pest and the disturbances it caused using both observational and remote sensing methods.

2.2. Data Collection

Data fusion is being increasingly used to generate time series with high temporal and spatial resolutions [1,25,39]. Multiyear, high-resolution data acquisition from different sensors (Figure 2) was conducted in order to create a database of phenophases denser than 8 to 16 days which has been the usual density for phenological time series in previous studies [40–42].
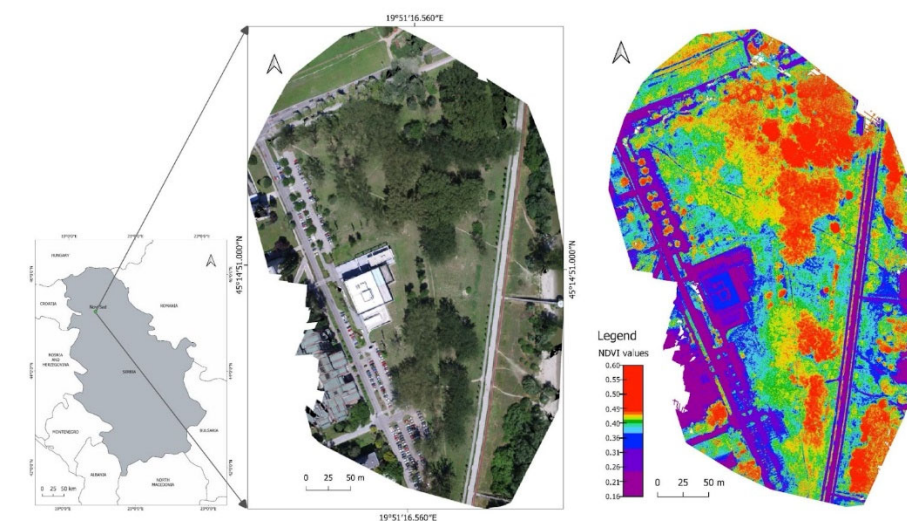
Figure 1. Aerial photo of the location of poplar tree stands: orthophoto image of the site by UAV and NDVI values calculated for the whole location.

Sensors \ Spectrum (nm)	blue	red						red edge						NIR						
	492.4	631	640	648	657	665	674	682	691	705	730	740	783	807	820	833	838	850	860	869
Sentinel 2 satellite (resolution 10×10m)	☐					664.6				(704.1)*		(740.5)*	(782.8)*			832.8				
Ximea hyperspectral camera (resolution 15×15cm)		☐	☐	☐	☐	☐	☐	☐	☐	☐	☐			☐	☐		☐	☐	☐	☐

Figure 2. Spectrum and resolution of sensors. * Sentinel-2 resolution in the red edge part of the spectrum is 20 × 20 m. Wavelengths used for the calculation of vegetative indexes from Sentinel 2 images are marked in yellow, and those used for the calculation of vegetative indexes from hyperspectral camera are marked in red.

Sentinel-2 has a resolution of 20 × 20 m in the red edge part of the spectrum. Although resampling can be carried out as in previous research (i.e., [43,44]), due to the comparison of data from different sensors, we wanted to avoid any uncertainties coming from such a process and did not compare normalized difference red edge index (NDRE) acquired from the satellite with the NDRE calculated from hyperspectral data. Data integration was carried out using only normalized difference vegetation index (NDVI) time series. The data obtained by using a hyperspectral camera and satellite sensors differ in spatial and temporal resolution, which affects the accuracy of the measurements. Visual monitoring of phenology is the most frequent and can be carried out daily as it is not conditioned by external factors. Hyperspectral imaging is not possible if there is precipitation, while satellite images can only be used if they were taken on sunny days. The data obtained by measuring with a hyperspectral camera have a higher spatial resolution and, therefore, are expected to be the most accurate. Monitoring of phenology was performed daily from the beginning of the vegetation season. The frequency of hyperspectral camera recording was somewhat less frequent due to precipitation, especially at the beginning of the year. Satellite images have a high frequency (every 2–3 days on average), but it is only possible to use those taken on sunny days, which is only 30% (48 to 70 images a year).

2.2.1. Hyperspectral Imaging

Ximea xiSpec MQ022HG-IM-5X5-NIR was used for hyperspectral imaging from the rooftop of BioSense Institute from the same point with the same spectralon position (Figure 3). In order to ensure approximately the same lighting conditions in relation to the same angle of incident of sunlight towards the poplar trees, hyperspectral image acquisition was conducted with the sun at its zenith position (12 p.m. until the last weekend of March,

and 1 p.m. from the end of March onward due to daylight saving time). We focused on imaging the trees' side view with the region of interest (ROI) with an approximate size of 13.5 m × 10 m.

(**a**)   (**b**)
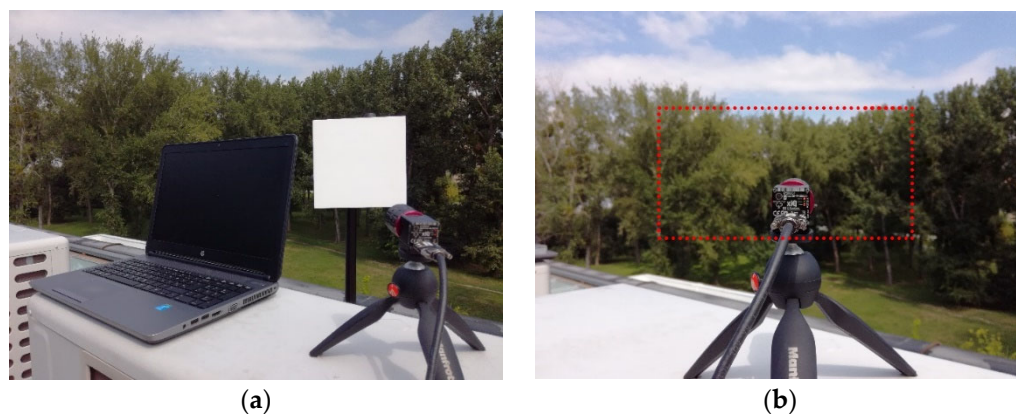
Figure 3. Hyperspectral imaging from the rooftop: (**a**) spectralon position and (**b**) ROI.

For each imaging, we made 3 shots: the spectralon covering the whole camera's field of view, the image of the trees' side view with the region of interest (ROI) 13.5 m × 10 m in size, and the image with the closed aperture.

One pixel corresponds to 15 cm^2 of the region of interest and 0.002 cm^2 of the spectralon. The camera registers 25 spectral channels and was used with a 600–875 nm filter which increases the sensitivity of the camera in the mentioned part of the spectrum. In this part of the spectrum, there are wavelengths of red (630–680 nm), red edge (680–730 nm), and near-infrared (750–1400 nm) which are used to calculate vegetation indices.

A broadband (400–1000 nm) anti-reflection (BBAR) coated lens with fixed focal length f = 35 mm and a set aperture of f/2.8, together with a bandpass filter (600–875 nm) from Edmund Optics, was mounted on a Ximea xiSpec MQ022HG-IM-5X5-NIR hyperspectral snapshot mosaic USB3 camera model and was used during the image acquisition procedure. The camera consisted of a CMOS CMV2000 sensor with a physical pixel size of 5.5 μm × 5.5 μm and a native resolution of 2048 × 1088, on which, at a wafer level on top of the pixel structure, were placed 25 hyperspectral filters based on a Fabry–Pérot structure and with an active range in near-infrared light between 665 nm and 960 nm. With the CMV2000 (CMV2K) sensor with an optical size of 2/3″ and BBAR lens with fixed focal length, a horizontal field of view (FOV) of 18.3°, vertical FOV of 9.8°, and a working distance (WD) of 165 mm–∞ were achieved.

The filters were organized in a snapshot mosaic 5 × 5 layout (SSM5x5), which was continuously repeated on the surface of the sensor, resulting in an approximate spatial resolution of 409 × 217 pixels. In Table 1, we report quantum efficiency (QE) in percentage of the filter responses in the red, red edge, and near-infrared parts of the light spectrum together with the used bandpass filter. According to the manufacturer's technical documentation, the central peak wavelengths of the spectral bands in Table 1 have a maximum relative deviation of ±1.0%. This created sensor, produced by Imec, is named IMEC CMV2K-SSM5x5-NIR. The quantum efficiency for Ximea xiSpec goes up to a 19% maximum.

The images of the hyperspectral camera were calibrated by making an image of the spectralon (which reflects 95% of the spectrum)—"white image"—and by closing the aperture, making a "black image" (Figure 4). The spectrum is calculated in relation to these two reference values.

Table 1. Quantum efficiency (QE, %) of filter responses for selected spectral bands used in the calculation of vegetation indices.

Red (nm)	QE (%)	Red Edge (nm)	QE (%)	NIR (nm)	QE (%)
631	6	807	19	682	13
640	8	820	14	691	9
648	11	838	8	705	19
657	8	850	9	730	13
665	7	860	8		
674	18	869	9		
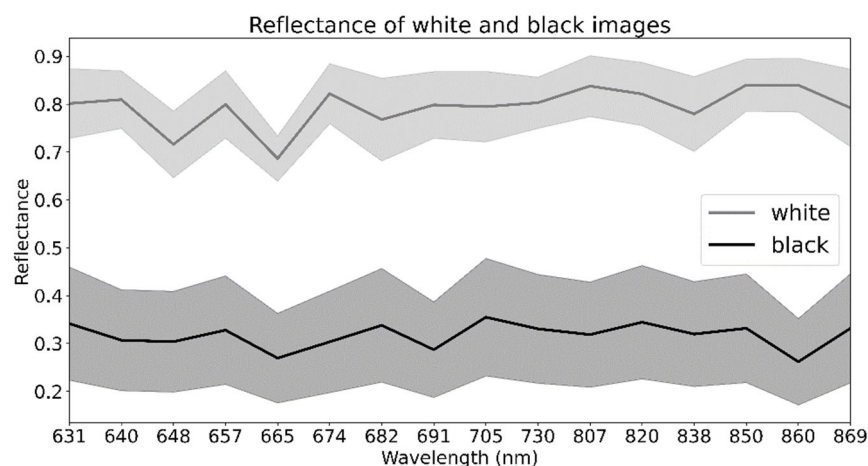
Figure 4. Reference spectra (mean values with standard deviation) calculated from "white" and "black" images for all considered wavelengths.

Another important feature of sensors for calculating spectral responses is quantum efficiency. Based on the quantum efficiency coefficients given by the camera manufacturer, the registered signals were interpolated. The low sensitivity of the instrument in certain parts of the spectrum means the possibility of a larger error in signal interpolation. Therefore, when calculating vegetation indices, it is important to use those wavelengths for which the quantum efficiency of the camera is higher, which in our case is for:

- wavelengths in the red spectral region 631 nm, 640 nm, 648 nm, 657 nm, 665 nm, and 674 nm;
- wavelengths in the near-infrared (NIR) spectral region 807 nm, 820 nm, 838 nm, 850 nm, 860 nm, and 869 nm;
- wavelengths in the red edge spectral region 682 nm, 691 nm, 705 nm, and 730 nm.

The closest range that both sensors cover in the red spectral region is around 665 nm, while Sentinel-2 registers the NIR spectral region around 833 nm and the Ximea hyperspectral camera around 838 nm. However, the quantum efficiency of the Ximea camera is the lowest in the aforementioned wavelengths (7% for 665 nm and 8% for 838 nm). Therefore, we used two parameters for choosing the corresponding wavelengths in the hyperspectral camera: (1) to increase the precision of the measurements for the calculation of the spectral response, we included wavelengths with better quantum efficiency in both red and NIR spectral regions; (2) although Sentinel-2 has a wide bandwidth in both spectral regions (31 nm in red and 106 nm in NIR), we have chosen the wavelengths of the hyperspectral camera within the range of Sentinel-2 coverage. For each part of the spectrum, the spectral response is calculated as follows: for red, the responses in 6 listed wavelengths were summed and an average was calculated and taken as a response in the red part of the spectrum. Likewise, red edge values were calculated as an average of the 4 wavelengths, and NIR as an average value of 6 values belonging to the corresponding part of the spectrum.

The hyperspectral raw measurements, obtained from the SSM5x5 sensor pattern (IMEC CMV2K-SSM5x5-NIR) from the Ximea xiSpec MQ022HG-IM-5X5-NIR camera with the gain 6, must go through several steps of calibration and correction before proper use. The steps are:

- offset removal;
- white–black reference correction;
- spectral correction;
- demosaicing.

The first step—offset removal—implies focusing on measurements obtained from an active sensor area with a width of 2045 pixels and height of 1080 pixels, for the SSM5x5 sensor pattern. This is achieved by excluding measurements at the edges of the sensor area with the original size in pixels of 2048 × 1088. Then, a final reflectance $R \in [0,1]$ for one of the spectral bands is obtained by conducting the following two-step white–black reference and spectral correction using the following equation:

$$R = \mathbb{C} \frac{(\rho - \rho_{b,\tau})}{\left(\rho_w - \rho_{b,\tau_{ref}}\right)} \frac{\tau_{ref}}{\tau},$$

where ρ represents the radiance of the object image, ρ_w, ρ_b are radiances of the white and black reference images, τ_ref and τ are integration times for the white reference image and object image, respectively, and $\mathbb{C}$ denotes spectral correction matrix. A correction matrix is defined as a part of a spectral correction process and it is applied after reflectance calculation. The spectral correction matrix is computed specifically for each combination of sensor and optical components (i.e., rejection filters, light source, etc.) and is provided in the sensor's calibration file. It is applied to the signal by multiplying the signal with the correction matrix [45]. The final step is the extraction of spectral bands of interest into separable images (matrices) from the original image consisting of repeated mosaic patterns of 5 × 5 per spatial pixel location (Figure 5). Namely, the sensor with 25 filters has a layout organized in 5 rows and 5 columns. Further, the vegetation index calculations can be conducted by performing simple matrix operations.
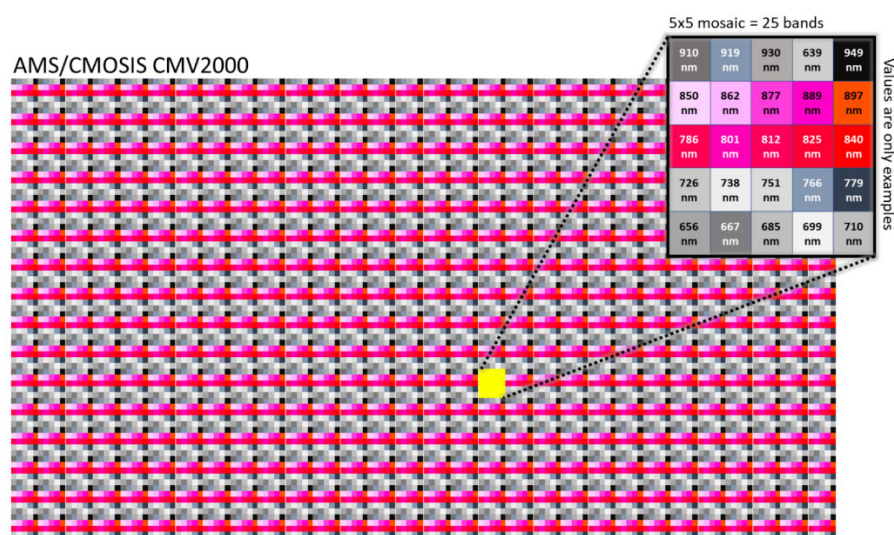
Figure 5. Snapshot mosaic pattern at sensor level for IMEC CMV2K-SSM5x5-NIR when no filter is used (source: https://www.ximea.com/downloads/usb3/manuals/xispec_technical_manual.pdf (accessed on 7 December 2022)).

This configuration is prone to noise from crosstalk induced by non-parallel light beams. Further noise is caused by dark current and vignetting effects as well as a chromatic

aberration of the optical setup. Additionally, the sensitivity in one pixel is not confined to one narrow wavelength band around the peak but has several minor peaks at other wavelengths. This latter effect can be accounted for by a so-called correction matrix. The major benefit of this sensor technology, namely, the combination of spectral as well as spatial resolution, comes with certain costs: comprehensive correction/calibration, reduced spatial and temporal resolution when compared to high-speed cameras, and reduced spectral resolution when compared to spectrometers. In the publication of Gerdes et al. [46], in Table 2, there is a list of the advantages and drawbacks of different sensor technologies that have been used for process monitoring in laser powder bed fusion. Snapshot hyperspectral imaging fills a niche and whose potential shall be discussed in the remainder of this article.

Table 2. Ground-based phenological observation for 2018, 2019, and 2020.

	Phenophase Duration (DOY)		
	2018	**2019**	**2020**
Flowering	40–84	39–77	62–93
Fruiting	85–124	78–114	94–136
Leafing	86–337	99–327	83–327
Leaf miner	93–141	136–157	114–136

2.2.2. Satellite Imaging

Vegetation indices for the same trees were calculated from Sentinel-2 (10 m × 10 m resolution) satellite images. The stands were georeferenced in QGIS (3.10.14) on the layer of Google Maps (Source: Map data 2022 © Google) and shape files were created. Further calculation of the indices was carried out according to the following formulas:

$$NDVI = \frac{(NIR - red)}{(NIR + red)}$$

$$EVI = G \times \frac{(NIR - red)}{(NIR + C1 \times red - C2 \times blue + L)}$$

A raster with the calculated values of vegetation indices was created and the data were extracted from the satellite images according to the shapefiles previously created.

Poplar crowns are more than 20 m wide and there is no subpixel variation. The NDVI was chosen because it can be calculated from both images of the Ximea xiSpec hyperspectral camera and from satellite images, and the values can be compared. NDVI is the most commonly used index in biological disciplines of remote sensing, but due to a large number of factors that affect its values (atmosphere, background, soil moisture, etc.), alternatives such as an optimized vegetation index (enhanced vegetation index—EVI) and others were developed. EVI should better represent the physiological processes in the plant, excluding the influence of external factors. The red edge part of the spectrum is used to calculate the NDRE index, which Sentinel-2 registers exclusively in the resolution of 20 m × 20 m. For the study area, this resolution is too low so it would give inaccurate results that would not be comparable to the results obtained by hyperspectral camera imaging.

Unlike the hyperspectral camera images, the Sentinel-2 images were already calibrated and atmospherically corrected, so the calculated values of the spectral responses were obtained. We used exclusively atmospherically corrected images (marked L2A) and excluded L1C to avoid inconsistencies in the data due to the differences in the process of atmospheric correction. The values of vegetation indices NDVI and EVI for a given area were obtained by overlapping images of the red and NIR part of the spectrum, according to the standard formula, using the QGIS program. The shape and position of the trees were marked on the orthophoto "Google Maps" (Source: Map data 2022 © Google) and then the vegetation indices were calculated according to their georeferenced position.

Only satellite images taken during sunny days were used to calculate vegetation indices. On cloudy days, the values of vegetation indices are reduced due to misreading of the spectral response caused by cloud reflection. Images in which the cloud is directly above the observed trees or creates a shadow on this surface were excluded.

2.2.3. Phenology

Phenology is categorized into 3 phenophases (leafing, flowering, and fruiting) and 3 subphases within each phenophase (beginning, full development, and end) [47]. We tracked the status and the intensity of the phenophase by dividing each phenophase into subphases based on the percentage of fully developed plant parts (flowers in the flowering phenophase, fruits in the fruiting phenophase, and leaves during the leafing phenophase) because they develop unevenly and should be regarded as processes [48]. The beginning of the flowering phenophase is the period from the opening of the flower buds to the moment of development of 80% of the flowers. Full development is seen from the development of >80% of flowers to the beginning of their decline, and for the very end, the period from the decline of >20% of flowers to the complete end of the phenophase is taken. In the same way, the phenophases of fruiting and leafing are divided into the beginning—the period until the moment of the development of 80% of plant parts—full development of phenophase when >80% of leaves or fruits are developed and the end of phenophase from the moment of decline >20% of plant parts until the complete end of the phenophase [49].

2.3. Data Analysis

The following software was used for the data collection and processing: PyCharm 2018.1 EAP JetBrains, Pix4D SA 4.0, Ximea CamTool, QGIS (3.10.14).

2.3.1. Calculating Vegetation Indices

The mean values and medians of the NDVI and NDRE index were calculated from the hyperspectral camera and satellite values of the spectral response. Normalized difference vegetation index (NDVI) was obtained from the ratio of the mean values of the most efficient NIR and red channels. Normalized difference red edge index (NDRE) was obtained from the ratio of the mean values of the most efficient red edge and NIR channels. The choice of indices calculated from the hyperspectral camera is determined by the wavelengths it registers and the characteristics of the sensor. For example, EVI, which uses the blue part of the spectrum not registered by the Ximea xiSpec camera, was not calculated.

In a hyperspectral camera, there are 25 channels for each pixel. Out of the chosen wavelengths that correspond to those of Sentinel-2 sensors, we calculated average values for the red, red edge, and NIR part of the spectrum and further applied the equation to calculate NDVI and NDRE values for each pixel. The images of vegetation index (VI) values were further denoised using only median values of VI to exclude the outliers. Thus, we eliminated the possibility that low index values of individual pixels significantly affected the mean value of vegetation indices.

2.3.2. Data Processing and Integration

The assumption is that each time series consists of systematic patterns (a set of identifiable components) and a random "noise" (error) that makes it difficult to identify the patterns. Most time series analyses involve some form of "noise" filtering to make a pattern visible [50]. Data smoothing methods are expected to maintain the integrity of vegetation dynamics while removing the noise component [51–54]. The first step in the signal analysis is the interpolation of the missing data. Time series analysis implies one of several methods—linear, polynomial (2nd, 3rd, 5th order), and spline. The next processing step is denoising and we used the Savitzky–Golay filter. Similarly to interpolation, the choice of the parameters (polynomial order and window) depended on the original data set. With satellite data, the temporal resolution was low and might have been even lower than 10 days at the beginning of the season (due to cloudy weather). This suggests

using a smaller window as flowering and fruiting phenophases might finish in less than 2 weeks. The parameters for the processing of hyperspectral data were chosen according to their temporal resolution and their relation to phenology. These processing steps reduced irregularities (random fluctuations) in the time series, which made it easier to observe the behavior of the series. It is also an effective means of predicting future time series values [50]. We compared all the methods in interpolation: linear, spline, and polynomial transformation (2nd, 3rd, and 5th order).

Our setup of nadiral and lateral imaging was identical to that of Zhou et al., 2021 [22]. Satellite images were in the nadiral position, and lateral images from the hyperspectral camera were separated into 3 layers, namely the upper, middle, and lower part of the crown, to compare if there are differences in the contribution to the vegetation indices of various parts of canopies. Ye et al. [55] proposed a similar setup (lateral imaging (NDVI image)) for spectral analysis for the purposes of the estimation of nitrogen content and found that this method can successfully be used at the canopy level. Relating airborne and ground-based hyperspectral images allows taking advantage of the spatial characteristics of the former and the spectral responses of the latter. This setup is mostly used in orchards [56–58], although several studies explored the differences in the vegetation indices in mid-crown [59] and below-crown imaging [60]. All the researchers found these setups to be justified and give reasonable results. Ali et al. also found that Sentinel-2 imagery is complementary to that collected from the ground and used processing steps similar to our study (polynomial fitting and linear extrapolation). Raheja et al. [61] found high correlations between NDVI from hyperspectral sensors of lateral imaging and a spectroradiometer from an airborne sensor while Fan et al. [62] found that hyperspectral imaging with the proper image processing could detect the quality changes between and within canopies.

2.3.3. Calibration of Remote Sensing Data Using Proximal Observations

Data collected by in situ measurements (hyperspectral imaging, phenological monitoring) were used to calibrate data collected by remote sensing—satellite images (i.e., to relate the exact part of the VI curve with the corresponding phenophase). For the temporal alignment of the 3 data sets, we acquired data on the same date or 1 day apart from each other. In the example of 2018, we see that out of 49 satellite images, 26 were aligned with hyperspectral imaging (Figure 6). Hyperspectral imaging was limited by the weather condition (precipitation), but the data were collected within the day from satellite passages. Only 3 satellite images (in July) were more than 1 day apart from the hyperspectral images. There are 127 hyperspectral images during the vegetative season that lasted 294 days. The following years are as follows: in 2019—51 satellite and 130 hyperspectral images and in 2020—70 satellite and 77 hyperspectral images. In the year 2020, the COVID-19 outbreak caused restricted visits to the laboratory and restricted availability of the equipment and it significantly hampered temporal resolution of the acquisition by the hyperspectral camera.

Fusion of the data from the nadiral point of view with the ground-based ones has been explored before [22,55,61]. Ali et al. [60] found that the data from Sentinel-2 and the ground-based ones from the hyperspectral camera (laterally made) are complementary. Our setup included calculation of the indices (NDVI and EVI in satellite data, and NDVI and NDRE in hyperspectral data) and comparison of the indices' correlation among themselves and relation to the phenology of poplar trees. We explored the possibility of integrating NDVI values from both sensors into one timeline.

Temporal alignment of the data acquisition from different sensors (satellite and hyperspectral camera) allowed correlation of the data. The interpolation procedure was identical and all the dates were used for the calculation of the correlation.

After the fusion of the data, we could further remotely identify phenological phenomena of plants including the beginning, course, and end of phenophases, and monitor physiological changes—the presence of pests or disease. Time series of changes in spectral response in relation to the observed phenological changes were defined and the correla-

tion of changes in spectral response in relation to changes in phenophase intensity and physiological activity was calculated.

NDVI images for the observed areas were obtained by taking median values calculated for each pixel of the hyperspectral camera during the season and during the leaf miner attack. Poplar species attacked and not attacked by the leaf miner *Fenusella hortulana* (Klug, 1818) were monitored and changes in their indices were registered before, during, and after disease development.

Before statistical analysis, the data were tested by using the Shapiro–Wilk test, a standard formal test for assessing normality recommended for small and medium samples [63], which confirmed the application of non-parametric statistics tests was needed. Spearman's test [64] analyzed the extent to which NDVI values measured by remote and proximal measurements correlated to determine whether in situ measurements could be used to overcome the problem of low-frequency satellite imagery and the impossibility of using it during cloudy days. Differences in the average values of vegetation indices during leafing and during leaf miner attacks were analyzed using the Wilcoxon signed-rank test which is a non-parametric alternative to the paired sample *t*-test [65].
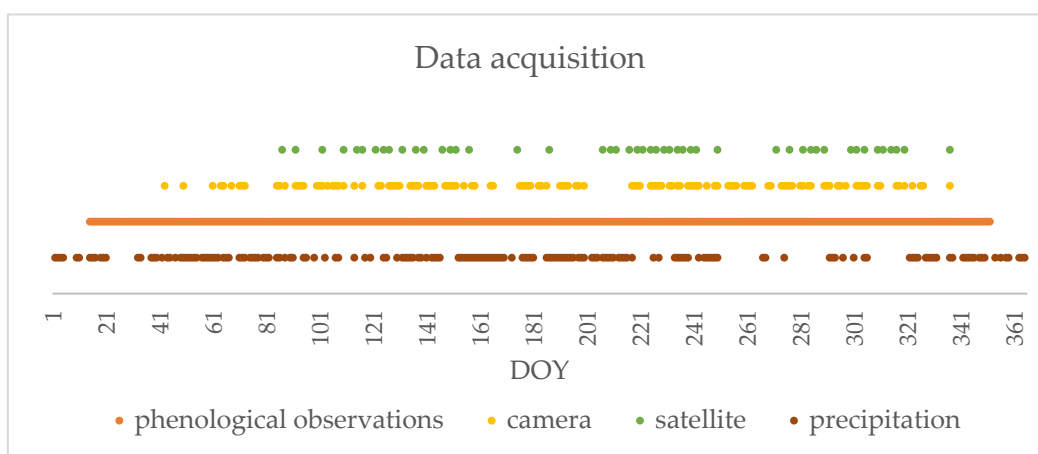
Figure 6. Daily precipitation and the frequency of data acquisition in 2018 by the hyperspectral camera, satellite, and phenological observations.

3. Results

3.1. Phenology Data Acquisition

Phenological observations were made daily and throughout the year, according to the methodology previously described. Phenotables were created for flowering, fruiting, and leafing as well as for the leaf miner attack. Leaf miners were detected with the first visible symptoms of the disease—the marks on the leaves. The vegetation season lasted 297, 288, and 265 days in 2018, 2019, and 2020, respectively (Table 2). Flowering occurred latest in 2020 but the leafing season was the longest. The intensity of leaf miner disturbance differed among years and was the strongest in 2018, with the major defoliation appearing during the leafing phenophase, and the weakest in 2020 when leaves were only partially damaged.

Some authors [66–68] suggested that phenology might differ in the upper, middle, and lower part of the crown and we acquired data by segmenting the canopies and creating phenotables for each part of the crown separately. Our research showed no differences in the development of phenophases among different parts of the crown.

3.2. Remote Sensing Data Acquisition

Using local methods for denoising signals when analyzing intra-seasonal variations (e.g., in disturbance analyses) was previously suggested [69] because they are able to capture seasonal details, thus we interpolated data using linear, polynomial, and spline methods. Although all the interpolation methods still captured differences in vegetation

indices during the leaf miner occurrence and during different phenophases (Figure 7), the polynomial interpolation of 2nd order showed the strongest differences ($p < 0.05$) and is, therefore, shown in the figures for the representation of the remote sensing capture of phenophases and stress caused by *Fenusella hortulana* (Klug, 1818) on poplar trees. The correlations of the signals from the satellite and hyperspectral camera are based on the same processing method.

(**a**)

(**b**)
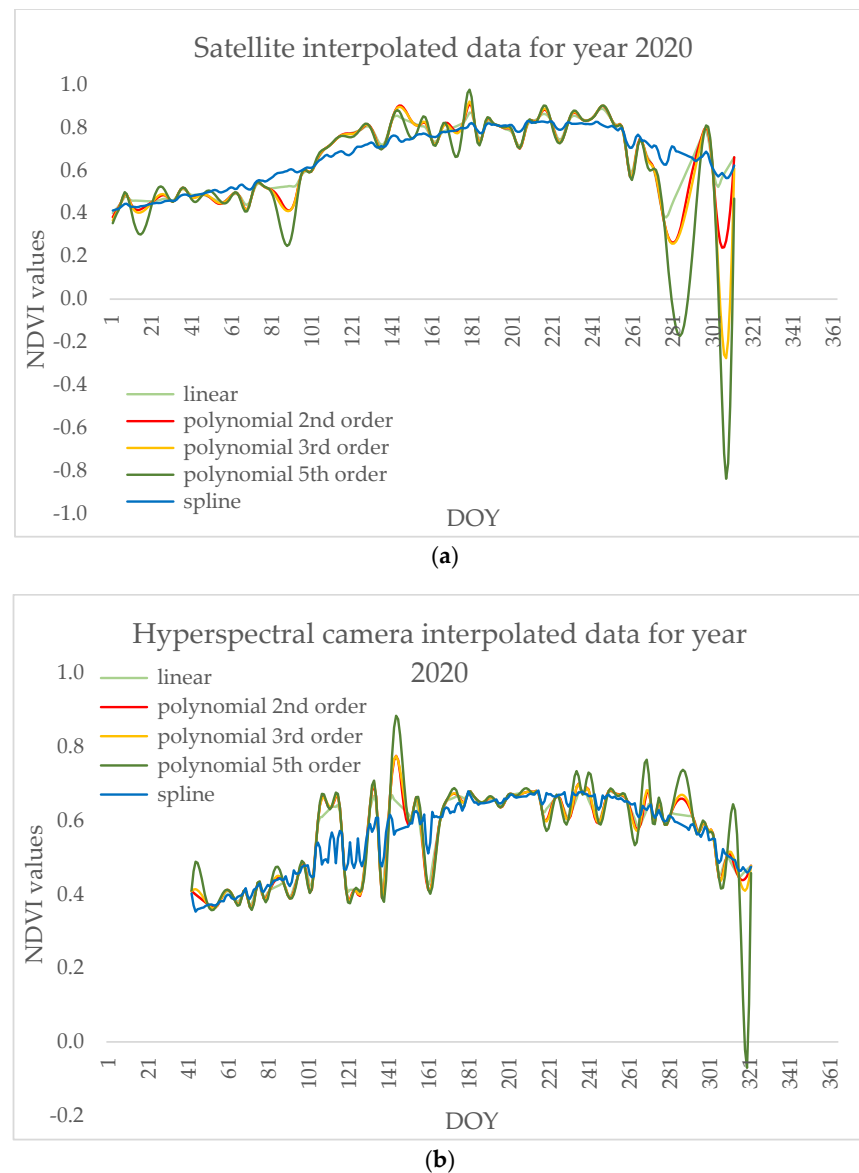
Figure 7. Data interpolated by linear, polynomial, and spline methods for (**a**) satellite and (**b**) hyperspectral camera.

3.2.1. Vegetation Indices from Satellite Sensors

The beginning of the season is characterized by intensive physiological processes, the beginning of the phenophase of flowering, and the development of pollen. After the flowers fall, the phenophase of fruiting has lower average values of vegetation indices (NDVI: 0.46 in 2018, 0.40 in 2019, 0.41 in 2020), which grow with the development of leaf buds and leaves (Figure 8).

Figure 8. *Cont.*

(c)
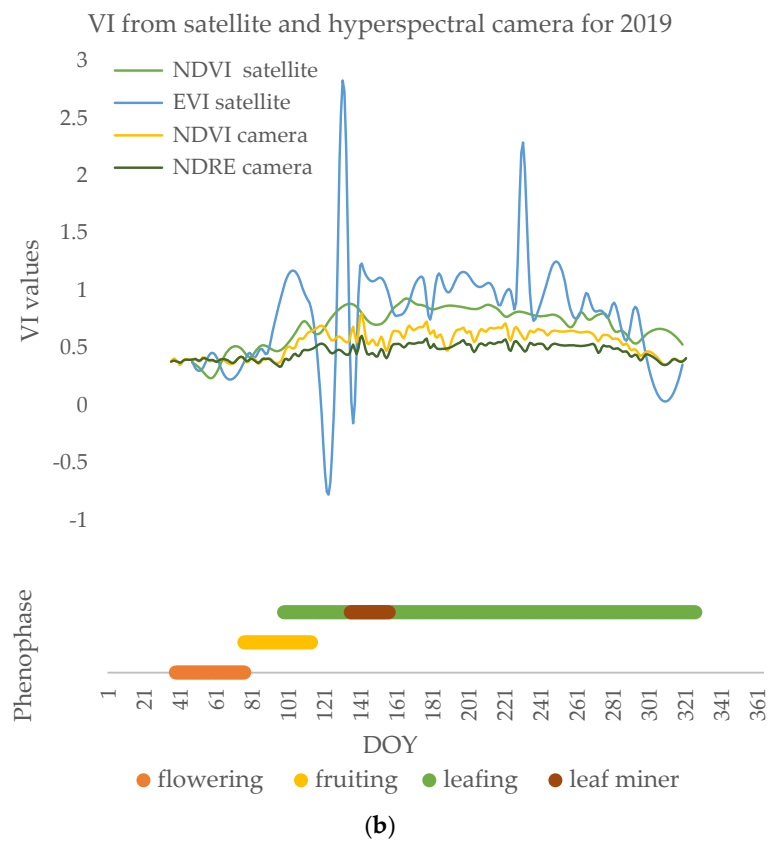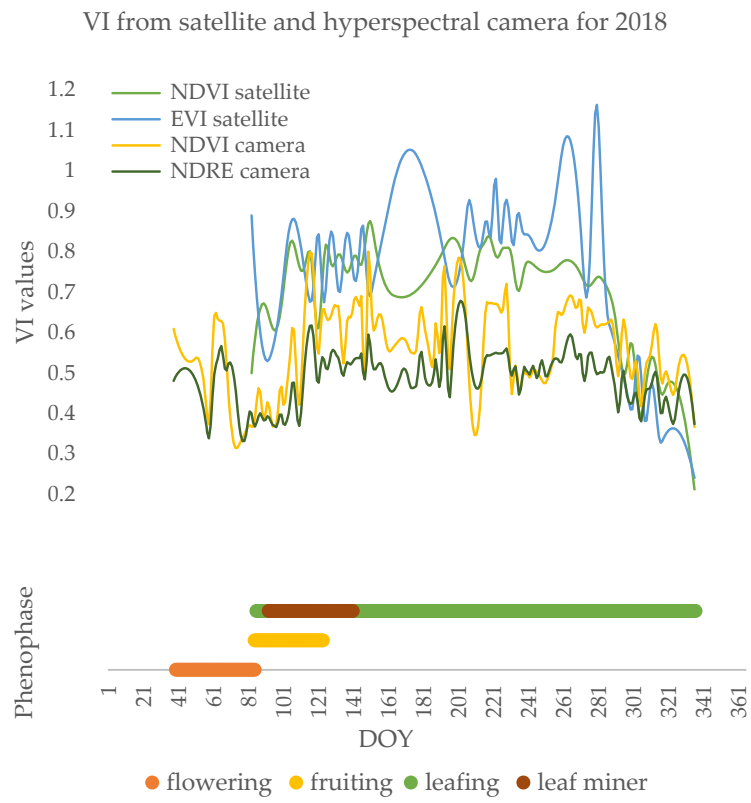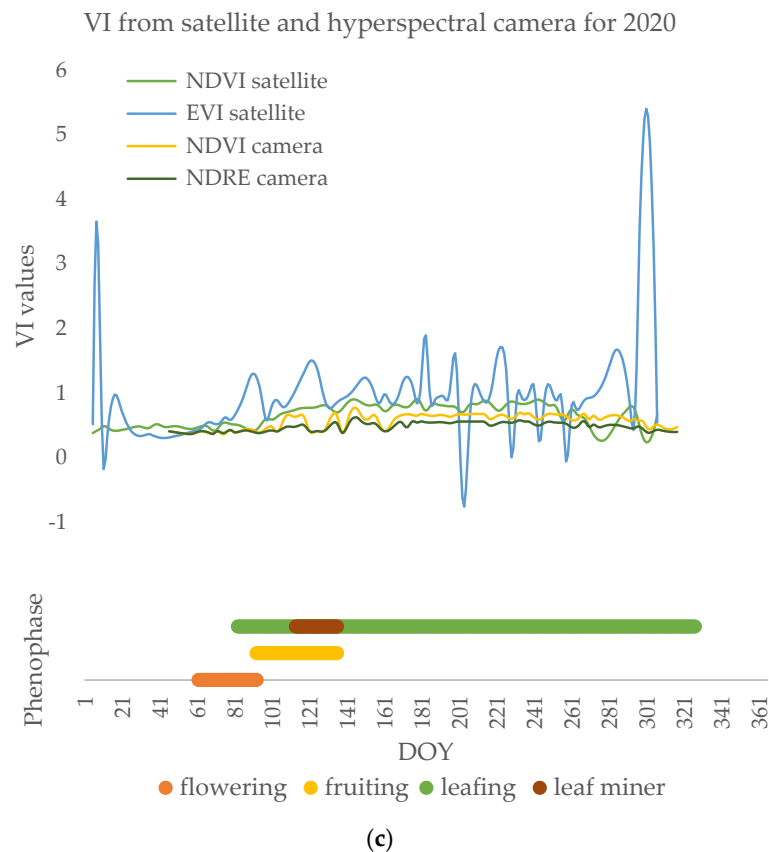
Figure 8. Annual time series of vegetation indices (i.e., NDVI and EVI from satellite and NDVI and NDRE from the hyperspectral camera) and the result of phenological observations in (**a**) 2018, (**b**) 2019, (**c**) 2020.

Poplars' NDVI values are expected to show a tendency of growing during the vegetation season starting from lower values at the beginning of the flowering phenophase with an increase during leaf development and another fall with leaf senescence. With the appearance of leaves, black poplar is attacked by leaf miners, causing the vegetation indices to decrease (Figure 8) before and during defoliation compared to the full leafing phenophase (NDVI: 0.48 in 2018, 0.40 in 2019, 0.50 in 2020), and increase with the development of new leaves. During the phenophase of full leaf development, NDVI satellite measurements have stable values around 0.8 with slight variations. In spring, clouds limit the number of images to only a few during the leaf miner attack. Due to the low frequency of imaging, the leaf miner attack could not be detected from the satellite images. Satellite images showed no significant differences during the phase of the feeding of the leaf miners ($p > 0.05$), but only during the defoliation (in the days after the leaf miner occurrence) ($p < 0.01$) (Figure 8).

Apart from NDVI, EVIs were calculated from the Sentinel-2 satellite images. Figure 8 shows their mean values throughout the years. These two vegetation indices vary in different ways during the season and differ significantly ($p < 0.01$) each year. By definition, the EVI is specifically tailored to separate the canopy signal from the background by reducing the influence of atmospheric characteristics on the index values. Still, there were no significant relations between its values and phenophases of the poplars ($p > 0.05$). On average, NDVI values were 0.68 in three successive years, while EVI was 0.81. A lack of satellite imaging is visible in the year 2018 when the full phenophase of flowering was missed due to cloudy weather.

3.2.2. Vegetation Indices from Hyperspectral Camera

The NDRE index has fewer oscillations and more stable values, but also significantly ($p < 0.01$) lower index values compared to NDVI (0.48 in 2018, 0.47 in 2019, 0.47 in 2020) (Figure 8). Deviations of the median from the mean values are not statistically significant and are greatest for the NDRE index at the beginning of the growing season when these values are low (standard deviation 0.02, 0.04, and 0.06). During the phenophase of leafing, which lasts from the end of March until the end of November, NDVI values are at their peak (Figure 8). A decrease in the values of NDVI and NDRE indices was observed during this phenophase, and the cause of the low values was the changes in the leaves that occurred as a consequence of the leaf miner attack. The leaf miners appeared in May and differed in intensity throughout the years. In 2018, *Fenusella hortulana* (Klug, 1818) caused total defoliation in black poplar and a drop in vegetative indices (mean NDVI 0.52, mean NDRE 0.45) unlike the Canadian poplar whose indices had stable high values during the leafing phenophase (mean NDVI 0.58, mean NDRE 0.50). In 2019 and 2020, leaf miner damage was far lower and the leaves and the crowns were only partially affected. However, even in 2020 both NDVI and NDRE indices indicated the presence of the leaf miner, having significantly lower values during its attack (mean NDVI 0.47, mean NDRE 0.44; $p < 0.01$) detected by hyperspectral imaging.

3.3. Performance of Remote and Proximal Spectral Analysis in Identification of Defoliation

The values of NDVIs measured by the hyperspectral camera are significantly lower ($p < 0.01$) than those obtained from the satellite images (0.56 in 2018, 0.55 in 2019, 0.54 in 2020). NDVI values measured in both ways show the same trend during the growing season (Figure 8). The differences may be due to the sensitivity of the sensor as the sensitivity of the satellite sensor is far greater than the sensitivity of the hyperspectral camera which had consistently lower values. On cloudy days, the values can be equally low.

A high positive correlation was found between the mean values of the NDVI obtained by proximal measurement with the Ximea hyperspectral camera and remote sensing—values obtained by satellite imaging (Sentinel-2) (0.75, $p < 0.01$). The median NDVI values of the hyperspectral camera correlate better with the values obtained from satellite images. The highest correlation between proximal and remote sensing of the NDVI was obtained by eliminating cloudy days (0.78, $p < 0.01$).

While in satellite images, the time series Wilcoxon signed ranks test shows that the drop in NDVI values during leaf miner attack is almost significant, in hyperspectral images, differences are more visible and statistically significant (Figure 9). In 2018, differences are statistically significant in vegetative indices for both NDVI and NDRE mean and median values ($p < 0.01$) (Table 3, Figure 9). That year, the leaves were severely affected and it led to extensive defoliation.

Table 3. Wilcoxon signed ranks test for 2018 hyperspectral data.

	NDVIm_LM vs. NDVIm_L	NDVImed_LM vs. NDVImed_L	NDREm_LM vs. NDREm_L	NDREmed_LM vs. NDREmed_L
Z	−3.066 [a]	−3.066 [a]	−3.066 [a]	−3.074 [a]
Asymp. Sig. (2-tailed)	0.002	0.002	0.002	0.002

[a]. Based on negative ranks. NDVI_L—NDVI mean values during leafing phenophase. NDVIm_LM—NDVI mean values during leaf miner attack. NDVImed_L—NDVI median values during leafing phenophase. NDVImed_LM—NDVI median values during leaf miner attack. NDREm_L—NDRE mean values during leafing phenophase. NDREm_LM—NDRE mean values during leaf miner attack. NDREmed_L—NDRE median values during leafing phenophase. NDREmed_LM—NDRE median values during leaf miner attack.
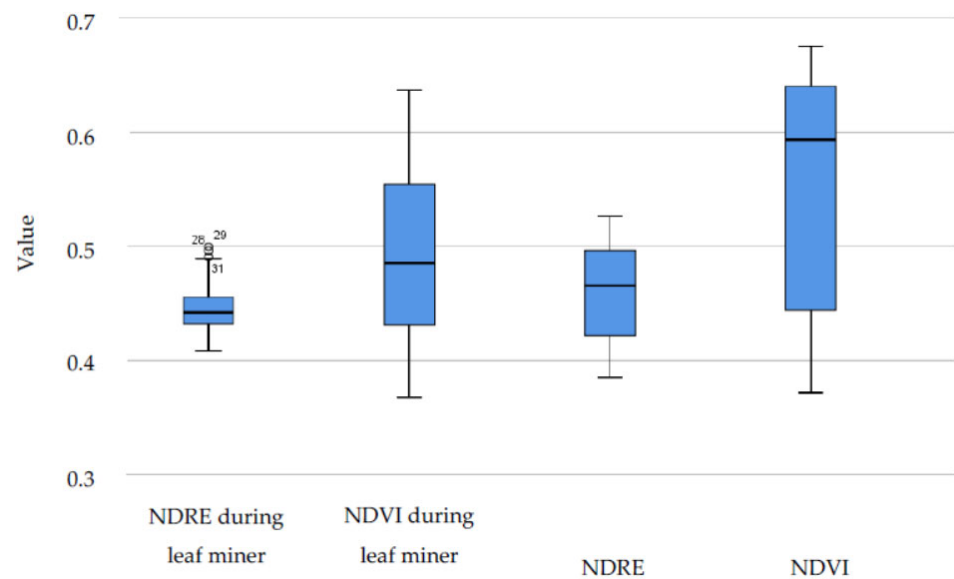
Figure 9. NDVI and NDRE hyperspectral data for the whole season and during leaf miner attack in 2018.

In 2019, the leaf miner attack was remotely detected and its presence was determined in phenological observations in a short period starting in May. Both NDVI and EVI satellite data values were significantly lower during the leaf miner attack ($p < 0.01$). Significant differences in vegetative activity were found between the peak of the leafing phenophase and the phase of leaf miner attack for mean NDVI and NDRE values ($p < 0.05$) (Table 4, Figure 10).

During 2020, leaf miners were detected both with phenological observations and hyperspectral imaging. Satellite data showed significantly lower NDVI values during the pests' presence while EVI failed to recognize the changes in vegetative activity. The most sensitive vegetative index was NDRE which detected significant differences between leafing phenophase and the period of leaf miner attack ($p < 0.05$) (Table 5, Figure 11).
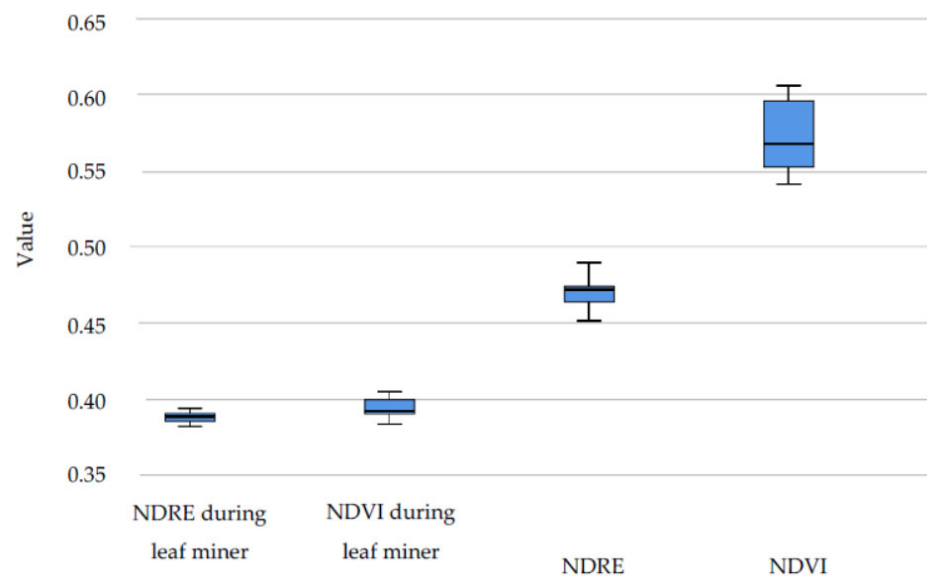
Figure 10. NDVI and NDRE hyperspectral data for the whole season and during leaf miner attack in 2019.

Table 4. Wilcoxon signed ranks test for 2019 hyperspectral data.

	NDVIm_LM vs. NDVIm_L	NDVImed_LM vs. NDVImed_L	NDREm_LM vs. NDREm_L	NDREmed_LM vs. NDREmed_L
Z	−2.197 [a]	−2.197 [a]	−1.961 [a]	−1.804 [a]
Asymp. Sig. (2-tailed)	0.028	0.028	0.050	0.071

[a]. Based on negative ranks. NDVIm_L—NDVI mean values during leafing phenophase. NDVIm_LM—NDVI mean values during leaf miner attack. NDVImed_L—NDVI median values during leafing phenophase. NDVImed_LM—NDVI median values during leaf miner attack. NDREm_L—NDRE mean values during leafing phenophase. NDREm_LM—NDRE mean values during leaf miner attack. NDREmed_L—NDRE median values during leafing phenophase. NDREmed_LM—NDRE median values during leaf miner attack.

Table 5. Wilcoxon signed ranks test for 2020 hyperspectral data.

	NDVIm_LM vs. NDVIm_L	NDVImed_LM vs. NDVImed_L	NDREm_LM vs. NDREm_L	NDREmed_LM vs. NDREmed_L
Z	−0.944 [a]	−0.674 [a]	−2.023 [a]	−2.023 [a]
Asymp. Sig. (2-tailed)	0.345	0.500	0.043	0.043

[a]. Based on negative ranks. NDVIm_L—NDVI mean values during leafing phenophase. NDVIm_LM—NDVI mean values during leaf miner attack. NDVImed_L—NDVI median values during leafing phenophase. NDVImed_LM—NDVI median values during leaf miner attack. NDREm_L—NDRE mean values during leafing phenophase. NDREm_LM—NDRE mean values during leaf miner attack. NDREmed_L—NDRE median values during leafing phenophase. NDREmed_LM—NDRE median values during leaf miner attack.
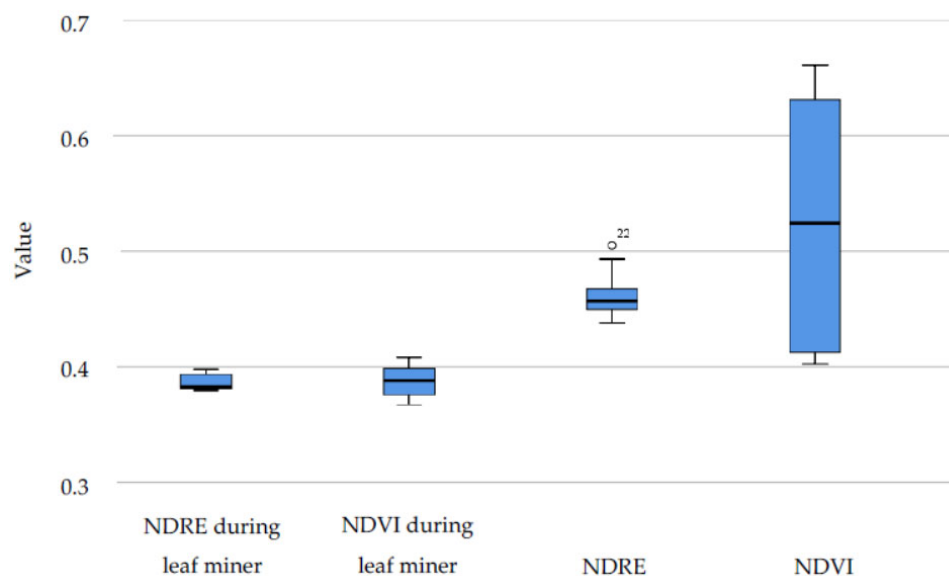
Figure 11. NDVI and NDRE hyperspectral data for the whole season and during leaf miner attack in 2020.

Remote sensing, during the phenophase of leafing, shows changes in NDVI values caused by leaf miner occurrence with statistical significance of $p < 0.05$ for vegetative indices in 2018 and 2019, while in 2020 changes were detected only in NDRE mean and median indices from the hyperspectral camera ($p < 0.05$). This indicates NDRE is the more sensitive tool for leaf miner detection.

The years 2018 and 2019 differ in spectral response as the defoliation occurred in the first year while, in the second year, poplars' leaves were less damaged by the leaf miners and the second foliation did not take place.

Results indicate insignificant differences among the 3 years ($p > 0.05$) as there were no phenological differences in poplars' observations.

Leaf miner attack differs in intensity, being the strongest in 2018, followed by defoliation, and less severe in the following years. Time series do not show these differences. On the seasonal scale, they were registered in all the years with different significance levels.

As the degree of damage by leaf miners differs over the years, the results show that small changes could be registered only by more sensitive tools and indices. Still, the forecast of the leaf miner attack could not be made as there were no indications in the VI of their occurrence.

4. Discussion

Visual observations of phenology are related but not identical to remote sensing-based phenology monitoring as the satellites measure the vegetative activity of plants and not the phenological events [19,70–72]. Researchers have turned towards mathematical theories, which limits the accuracy of specific phenological metrics' detection as these methods do not have a physiological basis [40]. This ambiguity in methodology generates a wide discrepancy in the timings estimated for the phenology metrics, making it difficult to compare them and determine the most applicable method for a specific use [73]. Therefore, we have chosen the traditional phenology metrics where the beginning, full development, and end of phenophases are recognized according to the percentage of the plant parts developed or fallen. This method proved to be fruitful as flowering and fruiting phenophases differ significantly from leafing phenophase and are clearly distinct from it ($p < 0.01$) for both VIs (NDVI and NDRE) even though the leafing phase includes the drop in values in spring due to leaf miner attack.

Physical models have an explicit mechanism that can simulate the phenological stages based on the individual plants [74,75]. This is especially important for filling in the scale gap that exists between plant and pixel. Still, satellites are the only tool for continuous and objective monitoring of Earth dynamics at all scales [76,77], and therefore overbridging the differences between the data from different sensors stays in the focus of current research. In addition, combined methods that incorporate remote sensing data and physical/empirical models offer great potential for improving vegetation phenology detection at larger scales.

Our work emphasizes the joint analyses of observation from multiple sources and multiple scales to bridge the relationship between remotely sensed phenology products and plant physiological processes, and improves our understanding of how the phenological transitions can be reflected from the pixel level. The spectral signal observed by sensors carried on satellites resolves the problem recognized by several researchers before [78–80]. Furthermore, the number of ground-based observations is insufficient, especially in underdeveloped and developing countries such as Serbia, that lack traditional phenological observing networks. In this regard, this research aims to remove discrepancies and integrate data into a broader phenological network.

Bridging the spatial mismatch between field and satellite data of different vegetation indices and different viewing angles of the observations was detected as another source of drawbacks of remote sensing techniques [76,81]. Satellites and near-surface sensors (except for the UAV) differ in the view angle and, as a result, near-surface sensors receive a higher contribution from the understory vegetation and a smaller contribution from the canopy top [76,77,81,82]. Despite the above, our results from satellite-based observations and the hyperspectral camera positioned lateral to poplar trees correlated well and had the same trends. The experiment was set so that the targeted tree was fully covering the field of view of the hyperspectral camera on one hand and corresponded to the pixels of the Sentinel images on the other hand. This method of monitoring shows that this issue might be resolved by proper setup and ground-truth data collection. Other research also showed that novel, low-cost remote sensing technologies based on individual tree analysis and calibrated remote sensing imagery offer great potential for affordable and timely assessments of the health condition of vulnerable urban forests [14]. The creation of a more effective and consistent method for monitoring urban forests' phenological and physiological changes will allow adequate calibration of remote-sensed data. Resolving

these issues and developing novel methods of calibration by ground-truth data can help integrate remote sensing techniques in forest management and the detection of insect disturbances might be included in ecosystem models [30]. Furthermore, researchers show that using in situ measurements of vegetative indices for calibration of satellite images could be improved by multilayer canopy measurements for better interpretation of the results as phenology differs between the lower, middle, and upper layer of the tree crown [18,22,59], thus we compared lateral and zenith imaging.

Satellite observations are based on the signal collected from the whole canopy while field observations are related to individual trees. These discrepancies create uncertainty in the measurements [34,83–85] that can be treated by the choice of the same optical principles for both sensors [84,86]. Even though the correlations between the VI values of both sensors were high, they were further improved with the choice of the same wavelengths for the calculation of the vegetation indices. Even using the wavelengths in a similar range when the exact ones are not available improves the correlation between sensors and thus allows using different platforms to improve the time resolution of remote sensing data.

Springtime is characterized by a large number of cloudy days. It is also the time of the leaf miner occurrence. This limits the usage of satellite images for monitoring vegetative activities as the imaging is rare and may miss part of the season or the entire phenophase. From satellite images, NDVI and EVI were calculated. Although the EVI takes into account atmospheric and background properties to isolate the canopy signal, the results show that there are mostly no significant correlations with phenological changes in poplars. EVI also shows a tendency to grow during the season, but it is characterized by low values at the beginning of the season and occasionally an unexpected decline during the phenophase of leafing. Non-parametric tests show that this index cannot be used to detect phenophases of leafing and leaf miner attack. Other studies also indicate problems with large variations in the EVI during the season and between seasons, as well as inconsistencies in different environmental conditions [87,88]. Sims et al. [89] found that EVI has substantial variation in sensitivity across seasons and years and other researchers even found random variations in EVI values among months [84]. These intra-annual fluctuations are expected to change throughout the season [90]. Therefore, NDVI outperformed EVI in the detection of phenophases. The NDVI has large oscillations at the beginning of the vegetation season. Apart from the low temporal resolution, these oscillations contributed to the inability of satellite images to detect the beginning of the leaf miner attack. It was only after the defoliation started that the images showed a clear decrease in the values of the indices. As the early detection of disease is especially important for the prevention of the spread of the disease, we further tested hyperspectral imaging for calibration and fulfillment of the satellite imaging time series. The inconsistencies among seasons might be due to cloudy weather and the time of the leaf miner occurrence. With the denser time series at the beginning of the season, the chances of satellite data to detect phenological shifts improve significantly.

Differences between pest types evidently dictate the spectral properties and choice of sensors. According to previous research [30], defoliation of broadleaved and coniferous trees has been detected predominantly using a single spectral index (82% and 50%, respectively). For broadleaved species, NDVI was used in almost half of the studies. The NDVI is one of the most used indices in biological disciplines for vegetation monitoring. The great advantage of this index is that the response in the red and near-infrared part of the spectrum used for its calculation can be registered using a large number of cameras and from different platforms. To monitor the phenology and physiology of plants, various methods and devices were used to obtain the best index and way of monitoring vegetation. NDVI remains the most popular and has been widely used to discriminate healthy from senescent foliage in forest stands affected by insects' attack [15,29,91–93]. For this reason, we compared sensors starting from the calculation of the NDVI values.

The hyperspectral camera was used for the creation of dense reference data points during the vegetation seasons of 2018 to 2020. The high positive correlations of NDVI values

obtained by satellite imaging and hyperspectral camera imaging are highly significant and show that the methods can be used simultaneously and those proximal measurements can compensate for the lack of satellite measurements during cloudy days. The data obtained using these methods show the same trend, although the values of the NDVI recorded by the hyperspectral camera are consistently lower. This may be due to the technical properties of the sensor. This is especially visible on cloudy days or days with precipitation when, due to the atmosphere, the NDVI values from sensors were sometimes low. The correlation is slightly better when cloudy days are excluded and values obtained exclusively during sunny days are used. Therefore, spectral signature is recognized from both satellite and hyperspectral images and can be used to detect variations caused by vegetative changes in poplars. It should thus result in a higher chance of obtaining a cloud-free observation during the short period of leaf miner attack.

Vegetation indices NDVI and NDRE were calculated from 16 different wavelengths belonging to the corresponding part of the spectrum. Every index has a differently shaped histogram, tending in the case of NDVI to higher values, and for the NDRE to lower values. This is in accordance with the previous studies [42] where NDVI values were similarly higher and less sensitive to vegetative changes. In previous research, many alternatives to NDVI were tested, each citing a different basis for better performance. Some authors [94] suggested RENDVI due to being more sensitive to changes in chlorophyll and, thus, better for the detection of early stress. For certain physiological characteristics of plants, NDRE has been shown to be a better indicator than the NDVI [95–101]. The differences in calculation among the indices are apparent after their application to the study area. There were no statistically significant differences between the mean and the median values of these indices in our study ($p < 0.05$). However, similarly to previous research [102,103], the NDVI had large value oscillations at the beginning of the season unlike NDRE. These oscillations also occur when the camera is in the zenith position and during lateral shooting of the plants. Following the phenology during the whole season in all layers of the tree crown separately gives additional information on the variations of the vegetative indices within one individual tree.

The oscillations have been observed in other studies in agricultural crops at the beginning of their season and even later in the spring, so the oscillations are not conditioned by weather but by physiological processes in the plant [104]. NDVI values varied during the season due to different causes. Serbia's air is extremely polluted so global dimming might cause changes in the NDVI [105]. Likewise, some oscillations are expected due to diurnal warming [106], human-associated activities [107], and an increase in CO_2 fertilization [108,109]. Medium and coarse spatial resolution sensors were most frequently used for mapping broadleaved defoliation, and researchers still found intra-annual time series analysis to be of crucial importance when studying these data sets [110,111]. Despite these issues, our study suggests that the median NDVI can be used to record the difference between leafing phenophase and the leaf miner attack although at a low level of significance, while mean NDVI values cannot be used to identify it except for the extreme cases such as defoliation. The medians exclude pixels that might be extreme and belong to the background, thus further eliminating the possibility of error. This is especially important in the spring when, due to bare branches, the background covers a large area of the image. Even though NDVI values showed a significant decrease only during the strong insect outbreak, their intra-annual variation could be further evaluated using different image processing or noise reduction methods to improve its performance for the years when the outbreak was weaker. Oscillations in the VI time series are expected and common. This further hampers the possibility to detect forest pests. Gartner et al. (Figure 3 in their paper) [28] illustrate the occurrence of the resprout in the same year after the insect disturbance. The overlapping period of the leaf development and the feeding of the leaf miner on the very same leaves create variability in the timeline where we can see the increase in VI values along with the appearance of the leaf miner. Only after the extensive damage is the drop in VI visible in the timeline. Gartner et al. also suggested that the distinction between trees

under disturbances and healthy trees is the best at the end of the first foliation and at the peak of the caterpillar feeding. Therefore, it is expected to see a decrease in vegetation indices only at the end of the leaf miner phenophase. Not until a string of days with low VI values is visible can we conclude the indications of disturbance in the plant.

The occurrence of hyperspectral cameras allowed the analysis of the "red edge" zone, to detect subtle changes in plant health, as occurs in the early stages of insect damage [112]. NDRE was the best-performing index in our study, it was the most sensitive and susceptible to subtle changes in vegetative activities. NDRE was superior, having lower intra-annual variations, although it showed slightly lower values compared to NDVI and EVI. The reason for this may be the technical properties of the camera which has a higher sensitivity in the red edge part of the spectrum (specified in the technical description of the camera) which is used to calculate the NDRE index and thus has higher accuracy in its measurement. Since the recording was performed at the same time every day, the differences in NDRE values from day to day indicate a seasonal change in physiological processes in plants. This confirms the statements by previous researchers [113] and observations by others [114] concerning the use of red edge and NIR reflectance as an indicator of forest health. In our study, the Wilcoxon signed rank test shows that the NDRE index is best for the detection of leaf miner attack in poplars. This is in line with the literature that cites NDRE as the best index for monitoring physiological processes in different species [95–101].

Possibilities of correlation of other indices obtained from different methods of poplar monitoring were considered. Comparison of NDRE indices obtained by the hyperspectral camera and satellite imaging was not possible due to different imaging resolutions. The resolution of satellite images in the red edge part of the spectrum is 20 × 20 m, which is too coarse for the single tree phenology observations and analysis. The EVI cannot be calculated from images from a hyperspectral camera because the camera does not register the blue part of the spectrum that is used for its calculation.

There are several issues to take into account when attributing the drop in VI to its cause. The end-of-season metric can be misidentified during an extended period of cloudiness, instead of corresponding to actual senescence [73]. Furthermore, challenges in leaf miner detection in broadleaved species are the differences in spectral responses between forest discoloration and insect defoliation [15,16]. Researchers [115] explain that the end of the leafing phenophase may also be mistaken for disease, water stress, or N stress. To be sure of the cause of changes in the indices, we combined multiple indices, multiple sensors, and multiple data sources to quantitatively describe annual patterns of vegetation phenology as an alternative as several previous studies suggested [116–118].

There is an increased need for forest monitoring at a finer spatial and temporal level and remote sensing is expected to fulfill these requirements [119]. Remote sensing of urban forests' defoliators could also allow retrospective analyses and predictive modeling in forest monitoring. Using a hyperspectral camera fills in the gaps of the satellite imagining and, therefore, allows the creation of time series dense enough to determine if the changes in VI are significant (eliminate the noise in signal), but only a few studies have used hyperspectral sensors to monitor defoliation in broadleaved forests [120,121]. As satellites might be used only on cloud-free days, using a hyperspectral camera significantly increases the density of the time series. In our research only ~30% of Sentinel-2 images were usable. Due to the ability of broadleaved trees to resprout in the same year after defoliation, a denser time series is of utter importance for the detection of defoliators [27–29]. This provides the possibility to detect the short period of maximum defoliation. The problem of reduced image availability reflects differently on phenophase detection depending on the period of the vegetation cycle [122]. Further improvement may move in the direction of better spatial resolution. Due to the aforementioned, we used a Ximea hyperspectral camera which is advanced in both spatial and temporal resolution compared to Sentinel-2.

Some studies even suggest that forest defoliation should be species- and region-specific, testing different sensors and combining different techniques for the best results. Therefore, we focused on an urban forest constructed solely of two poplar species. As

their spectral signature stayed the same throughout 3 years of observations ($p < 0.05$), it provided the basis for the analysis of the deviations from the time series and relation to defoliator outbreaks. The trends stayed the same as well, allowing us to relate oscillations during the leafing phenophase in April and May with its cause. Unlike in 2019 and 2020, in 2018 the values of vegetation indices decrease in the period after leaf miner attacks, reaching a minimum during the partial defoliation. This led to the exploration of whether the degree of leaf miner attack can be detected by remote sensing techniques. In the year 2018, by the end of May, the leaves resprouted, after which the values of vegetation indices grew and remained stable and on average the highest in the season. Out of two species of poplar, only the black poplar was attacked by the pest *Fenusella hortulana* (Klug, 1818), and the significant decline in the value of the indices during the attack of this leaf miner was clearly visible ($p < 0.05$). The indices of the Canadian poplar, which was not attacked by leaf miners, indicated stable values.

The difference in the intensity of the *Fenusella hortulana* (Klug, 1818) outbreaks over the years allows us to differentiate between defoliation and discoloration. This can be seen through the stronger difference in vegetation indices' values in 2018 when the defoliation occurred (decrease was more significant $p < 0.01$), unlike other years when the difference was visible but less significant and visible only in some of the VIs (NDRE $p < 0.05$). During the early stages of defoliation (when the worms are feeding on the tree), there are no visible signs of leaf miners' presence [123], whereas our images by the hyperspectral camera and satellite could already see the drop in the values of vegetative indices. The detection is characterized by the string of days with significantly lower values of the indices (mean values of NDVI and NDRE drop by 0.12–0.15 during the leaf miner attack compared to the average values in leafing phenophase). Although the reflectance of the vegetation among various sensors had the same trends, slight differences may still occur due to different view angles, illumination, and canopy density [95].

The problem of low spatial resolution has been addressed before in studies using Landsat intra-annual spectral variability [111] or fused products of varying sensors [28]. With the launching of the new Sentinel-2 satellite, image resolution is improved to 10 m for NDVI and 20 m for NDRE. Different resolution sensors can also be combined into one data set to increase the time series density [124]. Calibrating Sentinel-2 images with ground-truth data could be further used for historical data from Landsat and other sensors in order to provide long-term NDVI measurements. Sentinel-2 high spatial resolution imagery can thus significantly improve the creation of high-quality reference data sets for calibrating remote sensing models for detecting phenology and insect disturbances.

Similarly to other research, the results of this study clearly show that the collection of hyperspectral imagery provides a useful method to detect and monitor phenology and the symptoms resulting from forest defoliators' outbreaks. It further compares the accuracy of models created from high-resolution satellite imagery with those from the hyperspectral camera in the detection of physiological stress resulting from leaf miner outbreaks. This use of digital monitoring of vegetative activities has a wide application in a large number of disciplines (biology, forestry, medicine, plant protection, etc.) and the greatest benefits are economic profitability, impartiality, and accuracy in measurement as well as coverage of large areas.

Finally, real-time monitoring and short-term phenology prediction remain challenging. Short-term forecasting refers to the prediction before the occurrence of a phenological event, and real-time monitoring refers to the detection of a phenological occurrence as it occurs [19,73,125]. Our methodology failed to predict the occurrence of the leaf miner in advance but successfully determined its presence even when it caused different degrees of damage to trees.

5. Conclusions

The research created the basis for enabling the calibration of data collected by remote sensing (satellite images, hyperspectral images, and phenological observations) to iden-

tify phenological phenomena of plants including the beginning, course, and end of the vegetation phenophases and the leaf miner attack and its intensity.

The limitations of vegetation monitoring by satellite imagery are reflected in the limited number of vegetation indices that can be calculated (NDVI, EVI) as well as the problem of the influence of atmospheric phenomena and low time resolution. A hyperspectral camera can be used for overcoming these issues and integration of satellite imaging in the detection of defoliator outbreaks. The methodology is further improved when coordinating different sources and platforms using the same wavelengths. Once improved, these calibrated data can be used in combining different sensors and creation of prolonged time series, i.e., using Landsat data.

Targeting specific insect outbreaks determines the resolution and vegetation index. Choosing proper indices proved to be of utter importance for the detection of the VI changes and their causes in the vegetative activities of poplars. NDRE has the advantage of differentiating the vegetative changes due to leaf miner attack at the beginning of the outbreak as it is more sensitive than the NDVI and EVI. Thus, it was determined that these methods can also be used for remote detection and early detection of the disease.

The hyperspectral camera can thus be used for timely registration of the defoliators and detection of the potential severity of their hosts' damage. The angle of the imaging seemed to be unrelated to the values in VI as long as the field of view covered the same target. The high correlation between in situ measurements and remote sensing indicates the possibility of using ground-truth data for the calibration of the remote sensing monitoring of urban forests. Furthermore, this method can be applied in agricultural crops, ornamental species, etc. as it registers the physiological processes present in all plants.

We find that remote sensing methods have the advantage of offering broad-scale automated and repeatable methods for monitoring indicators of vegetation condition and, combined with detailed ecological site-based data, can improve urban forest management for further exploring ecological questions across a range of scales.

Author Contributions: I.S.: Conceptualization, Investigation, Formal analysis, Data curation, Writing—original draft, reviewing and editing; B.Š.: Conceptualization, Writing—reviewing and editing; M.P.: Conceptualization, Formal analysis; M.R.: Investigation, Writing—original draft; P.L.: Conceptualization, Formal analysis. All authors have read and agreed to the published version of the manuscript.

Funding: This work is supported through Ministry of Education, Science and Technological Development of Republic of Serbia (No. 451-03-68/2022-14/200358) and ANTARES project that has received funding from the European Union's Horizon 2020 research and innovation program under grant agreement SGA-CSA. No. 739570 under FPA No. 664387 (https://doi.org/10.3030/739570).

Data Availability Statement: All data underlining the results presented in this manuscript are available upon request to corresponding author.

Conflicts of Interest: The authors declare no conflict of interest.

References

1. Zheng, Y.; Wu, B.; Zhang, M.; Zeng, H. Crop Phenology Detection Using High Spatio-Temporal Resolution Data Fused from SPOT5 and MODIS Products. *Sensors* **2016**, *16*, 2099. [CrossRef] [PubMed]
2. Hmimina, G.; Dufrêne, E.; Pontailler, J.-Y.; Delpierre, N.; Aubinet, M.; Caquet, B.; De Grandcourt, A.; Burban, B.; Flechard, C.R.; Granier, A.; et al. Evaluation of the potential of MODIS satellite data to predict vegetation phenology in different biomes: An investigation using ground-based NDVI measurements. *Remote Sens. Environ.* **2013**, *132*, 145–158. [CrossRef]
3. Sonnentag, O.; Hufkens, K.; Teshera-Sterne, C.; Young, A.M.; Friedl, M.; Braswell, B.H.; Milliman, T.; O'Keefe, J.; Richardson, A.D. Digital repeat photography for phenological research in forest ecosystems. *Agric. For. Meteorol.* **2012**, *152*, 159–177. [CrossRef]
4. Fraser, R.H.; Latifovic, R. Mapping insect-induced tree defoliation and mortality using coarse spatial resolution satellite imagery. *Int. J. Remote Sens.* **2005**, *26*, 193–200. [CrossRef]
5. Wulder, M.; Franklin, S. *Understanding Forest Disturbance and Spatial Pattern: Remote Sensing and GIS Approaches*; CRC Press: Boca Raton, FL, USA, 2007.
6. West, P.W. *Aerial Signatures of Forest Insect and Disease Damage in the Western United States*; US Department of Agriculture, Forest Service, FHTET: Morgantown, WV, USA, 2006; ISBN 9788578110796.

7. Rullán-Silva, C.D.; Olthoff, A.; De La Mata, J.D.; Pajares, J.A. Remote Monitoring of Forest Insect Defoliation—A Review. *For. Syst.* **2013**, *22*, 377–391. [CrossRef]

8. Hall, R.; Skakun, R.; Arsenault, E. Remotely Sensed Data in the Mapping of Insect Defoliation. In *Understanding Forest Disturbance and Spatial Pattern: Remote Sensing and GIS Approaches*; CRC Press: Boca Raton, FL, USA, 2006; pp. 85–107. [CrossRef]

9. Wang, J.; Sammis, T.W.; Gutschick, V.P.; Gebremichael, M.; Dennis, S.O.; Harrison, R.E. Review of Satellite Remote Sensing Use in Forest Health Studies. *Open Geogr. J.* **2010**, *3*, 28–42. [CrossRef]

10. Adelabu, S.; Mutanga, O.; Azong, M. A Review of Remote Sensing of Insect Defoliation and Its Implications for the Detection and Mapping of *Imbrasia belina* Defoliation of Mopane Woodland. *Afr. J. Plant Sci. Biotechnol.* **2012**, *6*, 1–13.

11. Savastru, D.M.; Zoran, M.A.; Savastru, R.S.; Popa, I.R. Integrated Remote Sensing for Urban Forest Changes Monitoring. In Proceedings of the Sixth International Conference on Remote Sensing and Geoinformation of the Environment (RSCy2018), Paphos, Cyprus, 26–29 March 2018; Themistocleous, K., Papadavid, G., Michaelides, S., Ambrosia, V., Hadjimitsis, D.G., Eds.; SPIE: Bellingham, WA, USA, 2018; Volume 10773, pp. 223–235.

12. Soto, J.R.; Escobedo, F.J.; Khachatryan, H.; Adams, D.C. Consumer demand for urban forest ecosystem services and disservices: Examining trade-offs using choice experiments and best-worst scaling. *Ecosyst. Serv.* **2018**, *29*, 31–39. [CrossRef]

13. Sun, F.; Xiang, J.; Tao, Y.; Tong, C.; Che, Y. Mapping the social values for ecosystem services in urban green spaces: Integrating a visitor-employed photography method into SolVES. *Urban For. Urban Green.* **2018**, *38*, 105–113. [CrossRef]

14. Näsi, R.; Honkavaara, E.; Blomqvist, M.; Lyytikäinen-Saarenmaa, P.; Hakala, T.; Viljanen, N.; Kantola, T.; Holopainen, M. Remote sensing of bark beetle damage in urban forests at individual tree level using a novel hyperspectral camera from UAV and aircraft. *Urban For. Urban Green.* **2018**, *30*, 72–83. [CrossRef]

15. Jepsen, J.; Hagen, S.; Høgda, K.; Ims, R.; Karlsen, S.; Tømmervik, H.; Yoccoz, N. Monitoring the spatio-temporal dynamics of geometrid moth outbreaks in birch forest using MODIS-NDVI data. *Remote Sens. Environ.* **2009**, *113*, 1939–1947. [CrossRef]

16. Kantola, T.; Lyytikäinen-saarenmaa, P.; Vastaranta, M.; Kankare, V. Using High Density ALS Data in Plot Level Estimation of the Defoliation by the Common Pine Sawfly. In Proceedings of the SilviLaser 2011, 11th International Conference on LiDAR Applications for Assessing Forest Ecosystems, University of Tasmania, Hobart, Australia, 16–20 October 2011.

17. Kantola, T.; Vastaranta, M.; Yu, X.; Lyytikainen-Saarenmaa, P.; Holopainen, M.; Talvitie, M.; Kaasalainen, S.; Solberg, S.; Hyyppa, J. Classification of Defoliated Trees Using Tree-Level Airborne Laser Scanning Data Combined with Aerial Images. *Remote Sens.* **2010**, *2*, 2665–2679. [CrossRef]

18. Soudani, K.; Hmimina, G.; Delpierre, N.; Pontailler, J.-Y.; Aubinet, M.; Bonal, D.; Caquet, B.; de Grandcourt, A.; Burban, B.; Flechard, C.; et al. Ground-based Network of NDVI measurements for tracking temporal dynamics of canopy structure and vegetation phenology in different biomes. *Remote Sens. Environ.* **2012**, *123*, 234–245. [CrossRef]

19. White, M.A.; Nemani, R.R. Real-time monitoring and short-term forecasting of land surface phenology. *Remote Sens. Environ.* **2006**, *104*, 43–49. [CrossRef]

20. Liu, Y.; Wu, C.; Peng, D.; Xu, S.; Gonsamo, A.; Jassal, R.S.; Arain, M.A.; Lu, L.; Fang, B.; Chen, J.M. Improved modeling of land surface phenology using MODIS land surface reflectance and temperature at evergreen needleleaf forests of central North America. *Remote Sens. Environ.* **2016**, *176*, 152–162. [CrossRef]

21. Antonucci, S.; Rossi, S.; Deslauriers, A.; Morin, H.; Lombardi, F.; Marchetti, M.; Tognetti, R. Large-scale estimation of xylem phenology in black spruce through remote sensing. *Agric. For. Meteorol.* **2017**, *233*, 92–100. [CrossRef]

22. Zhou, J.-J.; Zhang, Y.-H.; Han, Z.-M.; Liu, X.-Y.; Jian, Y.-F.; Hu, C.-G.; Dian, Y.-Y. Evaluating the Performance of Hyperspectral Leaf Reflectance to Detect Water Stress and Estimation of Photosynthetic Capacities. *Remote Sens.* **2021**, *13*, 2160. [CrossRef]

23. Borgogno-Mondino, E.; Fissore, V. Reading Greenness in Urban Areas: Possible Roles of Phenological Metrics from the Copernicus HR-VPP Dataset. *Remote Sens.* **2022**, *14*, 4517. [CrossRef]

24. Gao, F.; Anderson, M.C.; Zhang, X.; Yang, Z.; Alfieri, J.G.; Kustas, W.P.; Mueller, R.; Johnson, D.M.; Prueger, J.H. Toward mapping crop progress at field scales through fusion of Landsat and MODIS imagery. *Remote Sens. Environ.* **2017**, *188*, 9–25. [CrossRef]

25. Walker, J.; de Beurs, K.; Wynne, R. Dryland vegetation phenology across an elevation gradient in Arizona, USA, investigated with fused MODIS and Landsat data. *Remote Sens. Environ.* **2014**, *144*, 85–97. [CrossRef]

26. Vrieling, A.; Meroni, M.; Darvishzadeh, R.; Skidmore, A.K.; Wang, T.; Zurita-Milla, R.; Oosterbeek, K.; O'Connor, B.; Paganini, M. Vegetation phenology from Sentinel-2 and field cameras for a Dutch barrier island. *Remote Sens. Environ.* **2018**, *215*, 517–529. [CrossRef]

27. De Beurs, K.; Townsend, P. Estimating the effect of gypsy moth defoliation using MODIS. *Remote Sens. Environ.* **2008**, *112*, 3983–3990. [CrossRef]

28. Gärtner, P.; Förster, M.; Kleinschmit, B. The benefit of synthetically generated RapidEye and Landsat 8 data fusion time series for riparian forest disturbance monitoring. *Remote Sens. Environ.* **2016**, *177*, 237–247. [CrossRef]

29. Spruce, J.P.; Sader, S.; Ryan, R.E.; Smoot, J.; Kuper, P.; Ross, K.; Prados, D.; Russell, J.; Gasser, G.; McKellip, R. Assessment of MODIS NDVI time series data products for detecting forest defoliation by gypsy moth outbreaks. *Remote Sens. Environ.* **2011**, *115*, 427–437. [CrossRef]

30. Senf, C.; Seidl, R.; Hostert, P. Remote sensing of forest insect disturbances: Current state and future directions. *Int. J. Appl. Earth Obs. Geoinf.* **2017**, *60*, 49–60. [CrossRef]

31. Hermosilla, T.; Wulder, M.A.; White, J.C.; Coops, N.C.; Hobart, G.W. Regional detection, characterization, and attribution of annual forest change from 1984 to 2012 using Landsat-derived time-series metrics. *Remote Sens. Environ.* **2015**, *170*, 121–132. [CrossRef]

32. Hilker, T.; Coops, N.; Gaulton, R.; Wulder, M.; Cranston, J.; Stenhouse, G.B. Biweekly disturbance capture and attribution: Case study in western Alberta grizzly bear habitat. *J. Appl. Remote Sens.* **2011**, *5*, 053568. [CrossRef]

33. Zhu, Z.; Woodcock, C.E.; Olofsson, P. Continuous monitoring of forest disturbance using all available Landsat imagery. *Remote Sens. Environ.* **2012**, *122*, 75–91. [CrossRef]

34. Zhang, X.; Wang, J.; Gao, F.; Liu, Y.; Schaaf, C.; Friedl, M.; Yu, Y.; Jayavelu, S.; Gray, J.; Liu, L.; et al. Exploration of scaling effects on coarse resolution land surface phenology. *Remote Sens. Environ.* **2017**, *190*, 318–330. [CrossRef]

35. Zhang, N.; Zhang, X.; Yang, G.; Zhu, C.; Huo, L.; Feng, H. Assessment of defoliation during the *Dendrolimus tabulaeformis* Tsai et Liu disaster outbreak using UAV-based hyperspectral images. *Remote Sens. Environ.* **2018**, *217*, 323–339. [CrossRef]

36. Feng, X.; Shao, Z.; Huang, X.; He, L.; Lv, X.; Zhuang, Q. Integrating Zhuhai-1 Hyperspectral Imagery With Sentinel-2 Multispectral Imagery to Improve High-Resolution Impervious Surface Area Mapping. *IEEE J. Sel. Top. Appl. Earth Obs. Remote Sens.* **2022**, *15*, 2410–2424. [CrossRef]

37. Dunjić, J.; Milošević, D.; Kojić, M.; Savić, S.; Lužanin, Z.; Šećerov, I.; Arsenović, D. Air Humidity Characteristics in "Local Climate Zones" of Novi Sad (Serbia) Based on Long-Term Data. *ISPRS Int. J. Geo-Inf.* **2021**, *10*, 810. [CrossRef]

38. Drekić, M.; Poljaković-Pajnik, L.; Pap, P.; Marković, M.; Vasić, V.; Pilipović, A. *Fenusela hortulana* (Hymenoptera: Tenthredinidae) nova štetočina topola u Srbiji/*Fenusela hortulana* (Hymenoptera: Tenthredinidae) new poplar pest in Serbia. *Biljn. Lek./Plant Dr.* **2016**, *44*, 162–167.

39. Gao, F.; Hilker, T.; Zhu, X.; Anderson, M.; Masek, J.; Wang, P.; Yang, Y. Fusing Landsat and MODIS Data for Vegetation Monitoring. *IEEE Geosci. Remote Sens. Mag.* **2015**, *3*, 47–60. [CrossRef]

40. Zeng, L.; Wardlow, B.D.; Xiang, D.; Hu, S.; Li, D. A review of vegetation phenological metrics extraction using time-series, multispectral satellite data. *Remote Sens. Environ.* **2020**, *237*, 111511. [CrossRef]

41. Simonetti, E.; Simonetti, D.; Preaton, D. *Phenology-Based Land Cover Classification Using Landsat 8 Time Series*; Publications Office of the European Union: Luxembourg, 2014; ISBN 978-92-79-40844-1.

42. Minařík, R.; Langhammer, J. Use of a Multispectral UAV Photogrammetry for Detection and Tracking of Forest Disturbance Dynamics. In Proceedings of the International Archives of the Photogrammetry, Remote Sensing and Spatial Information Sciences-ISPRS Archives, Prague, Czech Republic, 12–19 July 2016.

43. Kai, P.M.; de Oliveira, B.M.; Vieira, G.S.; Soares, F.; Costa, R.M. Effects of resampling image methods in sugarcane classification and the potential use of vegetation indices related to chlorophyll. In Proceedings of the 2021 IEEE 45th Annual Computers, Software, and Applications Conference (COMPSAC), Madrid, Spain, 12–16 July 2021; pp. 1526–1531. [CrossRef]

44. Mzid, N.; Castaldi, F.; Tolomio, M.; Pascucci, S.; Casa, R.; Pignatti, S. Evaluation of Agricultural Bare Soil Properties Retrieval from Landsat 8, Sentinel-2 and PRISMA Satellite Data. *Remote Sens.* **2022**, *14*, 714. [CrossRef]

45. Charle, W. Imec Hyperspectral Sensors. 2015. Available online: https://www.ximea.com/downloads/usb3/manuals/xispec_technical_manual.pdf (accessed on 7 December 2022).

46. Gerdes, N.; Hoff, C.; Hermsdorf, J.; Kaierle, S.; Overmeyer, L. Snapshot hyperspectral imaging for quality assurance in Laser Powder Bed Fusion. *Procedia CIRP* **2020**, *94*, 25–28. [CrossRef]

47. Denny, E.G.; Gerst, K.L.; Miller-Rushing, A.J.; Tierney, G.L.; Crimmins, T.M.; Enquist, C.A.F.; Guertin, P.; Rosemartin, A.H.; Schwartz, M.D.; Thomas, K.A.; et al. Standardized phenology monitoring methods to track plant and animal activity for science and resource management applications. *Int. J. Biometeorol.* **2014**, *58*, 591–601. [CrossRef]

48. Inouye, B.D.; Ehrlén, J.; Underwood, N. Phenology as a process rather than an event: From individual reaction norms to community metrics. *Ecol. Monogr.* **2018**, *89*, e01352. [CrossRef]

49. Simović, I.; Ocokoljić, M.; Obratov-Petković, D.; Vilotić, D. Genetic variability of bilaterally symmetric fruits of Norway maple in function of species biodiversity conservation. *Turk. J. Agric. For.* **2015**, *39*, 387–393. [CrossRef]

50. Shumway, R.; Stoffer, D. *Time Series Analysis and Its Applications with R Examples*; Springer: Berlin, Germany, 2011; Volume 9, ISBN 978-1-4419-7864-6.

51. Hermance, J.F. Stabilizing high-order, non-classical harmonic analysis of NDVI data for average annual models by damping model roughness. *Int. J. Remote Sens.* **2007**, *28*, 2801–2819. [CrossRef]

52. Cao, R.; Chen, J.; Shen, M.; Tang, Y. An improved logistic method for detecting spring vegetation phenology in grasslands from MODIS EVI time-series data. *Agric. For. Meteorol.* **2015**, *200*, 9–20. [CrossRef]

53. Beck, P.S.; Atzberger, C.; Høgda, K.A.; Johansen, B.; Skidmore, A.K. Improved monitoring of vegetation dynamics at very high latitudes: A new method using MODIS NDVI. *Remote Sens. Environ.* **2006**, *100*, 321–334. [CrossRef]

54. Hird, J.N.; McDermid, G.J. Noise reduction of NDVI time series: An empirical comparison of selected techniques. *Remote Sens. Environ.* **2009**, *113*, 248–258. [CrossRef]

55. Ye, X.; Abe, S.; Zhang, S. Estimation and mapping of nitrogen content in apple trees at leaf and canopy levels using hyperspectral imaging. *Precis. Agric.* **2019**, *21*, 198–225. [CrossRef]

56. Jang, K.E.; Kim, G.; Shin, M.H.; Cho, J.G.; Jeong, J.H.; Lee, S.K.; Kang, D.; Kim, J.G. Field Application of a Vis/NIR Hyperspectral Imaging System for Nondestructive Evaluation of Physicochemical Properties in 'Madoka' Peaches. *Plants* **2022**, *11*, 2327. [CrossRef]

57. Shao, Y.; Wang, Y.; Xuan, G. In-field and non-invasive determination of internal quality and ripeness stages of Feicheng peach using a portable hyperspectral imager. *Biosyst. Eng.* **2021**, *212*, 115–125. [CrossRef]

58. Wendel, A.; Underwood, J.; Walsh, K. Maturity estimation of mangoes using hyperspectral imaging from a ground based mobile platform. *Comput. Electron. Agric.* **2018**, *155*, 298–313. [CrossRef]

59. Ryu, Y.; Lee, G.; Jeon, S.; Song, Y.; Kimm, H. Monitoring multi-layer canopy spring phenology of temperate deciduous and evergreen forests using low-cost spectral sensors. *Remote Sens. Environ.* **2014**, *149*, 227–238. [CrossRef]

60. Ali, A.; Imran, M.; Ali, A.; Khan, M.A. Evaluating Sentinel-2 red edge through hyperspectral profiles for monitoring LAI & chlorophyll content of Kinnow Mandarin orchards. *Remote Sens. Appl. Soc. Environ.* **2022**, *26*, 100719. [CrossRef]

61. Raheja, A.; Espinas, A.; Dat, D.; Ezabadi, M.A.; Wolf, J.; Sherman, T.; Pham, F.; Bhandari, S.; Chaichi, M.R.; Green, R.L. Ground-truthing of UAV-based remote sensing data of citrus plants. *Proc. SPIE* **2018**, *10664*, 1066403. [CrossRef]

62. Wang, F.; Zhao, C.; Yang, H.; Jiang, H.; Li, L.; Yang, G. Non-destructive and in-site estimation of apple quality and maturity by hyperspectral imaging. *Comput. Electron. Agric.* **2022**, *195*, 106843. [CrossRef]

63. Garson, G.D. *Testing Statistical Assumptions*; Blue Book Series; Statistical Associates Publishing: Asheboro, NC, USA, 2012; pp. 1–52.

64. Spearman, C. The Proof and Measurement of Association between Two Things. *Am. J. Psychol.* **1987**, *100*, 441. [CrossRef]

65. Pallant, J. *SPSS Survival Manual: A Step by Step Guide to Data Analysis Using SPSS for Windows Version 15*; Routledge: London, UK, 2007.

66. Baldocchi, D.D.; Xu, L.; Kiang, N. How plant functional-type, weather, seasonal drought, and soil physical properties alter water and energy fluxes of an oak–grass savanna and an annual grassland. *Agric. For. Meteorol.* **2004**, *123*, 13–39. [CrossRef]

67. Pearcy, R.W. Sunflecks and Photosynthesis in Plant Canopies. *Annu. Rev. Plant Physiol. Plant Mol. Biol.* **1990**, *41*, 421–453. [CrossRef]

68. Seiwa, K. Advantages of early germination for growth and survival of seedlings of *Acer mono* under different overstorey phenologies in deciduous broad-leaved forests. *J. Ecol.* **1998**, *86*, 219–228. [CrossRef]

69. Cai, Z.; Jönsson, P.; Jin, H.; Eklundh, L. Performance of Smoothing Methods for Reconstructing NDVI Time-Series and Estimating Vegetation Phenology from MODIS Data. *Remote Sens.* **2017**, *9*, 1271. [CrossRef]

70. Atkinson, P.M.; Jeganathan, C.; Dash, J.; Atzberger, C. Inter-comparison of four models for smoothing satellite sensor time-series data to estimate vegetation phenology. *Remote Sens. Environ.* **2012**, *123*, 400–417. [CrossRef]

71. Verhegghen, A.; Bontemps, S.; Defourny, P. A global NDVI and EVI reference data set for land-surface phenology using 13 years of daily SPOT-VEGETATION observations. *Int. J. Remote Sens.* **2014**, *35*, 2440–2471. [CrossRef]

72. de Beurs, K.M.; Henebry, G.M. Land surface phenology and temperature variation in the International Geosphere-Biosphere Program high-latitude transects. *Glob. Chang. Biol.* **2005**, *11*, 779–790. [CrossRef]

73. de Beurs, K.M.; Henebry, G.M. Spatio-Temporal Statistical Methods for Modelling Land Surface Phenology. In *Phenological Research: Methods for Environmental and Climate Change Analysis*; Hudson, I.L., Keatley, M.R., Eds.; Springer: Dordrecht, The Netherlands, 2010; pp. 177–208. ISBN 978-90-481-3335-2.

74. White, M.A.; de Beurs, K.M.; Didan, K.; Inouye, D.W.; Richardson, A.D.; Jensen, O.P.; O'Keefe, J.; Zhang, G.; Nemani, R.R.; van Leeuwen, W.J.D.; et al. Intercomparison, interpretation, and assessment of spring phenology in North America estimated from remote sensing for 1982–2006. *Glob. Chang. Biol.* **2009**, *15*, 2335–2359. [CrossRef]

75. Zeng, L.; Wardlow, B.D.; Wang, R.; Shan, J.; Tadesse, T.; Hayes, M.J.; Li, D. A hybrid approach for detecting corn and soybean phenology with time-series MODIS data. *Remote Sens. Environ.* **2016**, *181*, 237–250. [CrossRef]

76. Berra, E.F.; Gaulton, R.; Barr, S. Assessing spring phenology of a temperate woodland: A multiscale comparison of ground, unmanned aerial vehicle and Landsat satellite observations. *Remote Sens. Environ.* **2019**, *223*, 229–242. [CrossRef]

77. Liu, L.; Zhang, X.; Yu, Y.; Guo, W. Real-time and short-term predictions of spring phenology in North America from VIIRS data. *Remote Sens. Environ.* **2017**, *194*, 89–99. [CrossRef]

78. Wingate, L.; Ogée, J.; Cremonese, E.; Filippa, G.; Mizunuma, T.; Migliavacca, M.; Moisy, C.; Wilkinson, M.; Moureaux, C.; Wohlfahrt, G.; et al. Interpreting canopy development and physiology using the EUROPhen camera network at flux sites. *Biogeosci. Discuss.* **2015**, *12*, 7979–8034. [CrossRef]

79. Migliavacca, M.; Galvagno, M.; Cremonese, E.; Rossini, M.; Meroni, M.; Sonnentag, O.; Cogliati, S.; Manca, G.; Diotri, F.; Busetto, L.; et al. Using digital repeat photography and eddy covariance data to model grassland phenology and photosynthetic CO_2 uptake. *Agric. For. Meteorol.* **2011**, *151*, 1325–1337. [CrossRef]

80. Richardson, A.D.; Jenkins, J.P.; Braswell, B.H.; Hollinger, D.Y.; Ollinger, S.V.; Smith, M.-L. Use of digital webcam images to track spring green-up in a deciduous broadleaf forest. *Oecologia* **2007**, *152*, 323–334. [CrossRef]

81. Hufkens, K.; Friedl, M.; Sonnentag, O.; Braswell, B.H.; Milliman, T.; Richardson, A.D. Linking near-surface and satellite remote sensing measurements of deciduous broadleaf forest phenology. *Remote Sens. Environ.* **2012**, *117*, 307–321. [CrossRef]

82. Peltoniemi, M.; Aurela, M.; Böttcher, K.; Kolari, P.; Loehr, J.; Hokkanen, T.; Karhu, J.; Linkosalmi, M.; Tanis, C.M.; Metsämäki, S.; et al. Networked web-cameras monitor congruent seasonal development of birches with phenological field observations. *Agric. For. Meteorol.* **2018**, *249*, 335–347. [CrossRef]

83. Liang, L.; Schwartz, M.D.; Fei, S. Validating satellite phenology through intensive ground observation and landscape scaling in a mixed seasonal forest. *Remote Sens. Environ.* **2011**, *115*, 143–157. [CrossRef]

84. de Moura, Y.M.; Galvão, L.S.; Hilker, T.; Wu, J.; Saleska, S.; do Amaral, C.H.; Nelson, B.W.; Lopes, A.P.; Wiedeman, K.K.; Prohaska, N.; et al. Spectral analysis of amazon canopy phenology during the dry season using a tower hyperspectral camera and modis observations. *ISPRS J. Photogramm. Remote Sens.* **2017**, *131*, 52–64. [CrossRef]

85. Fisher, J.I.; Mustard, J.F.; Vadeboncoeur, M.A. Green leaf phenology at Landsat resolution: Scaling from the field to the satellite. *Remote Sens. Environ.* **2006**, *100*, 265–279. [CrossRef]

86. D'Odorico, P.; Gonsamo, A.; Gough, C.M.; Bohrer, G.; Morison, J.; Wilkinson, M.; Hanson, P.J.; Gianelle, D.; Fuentes, J.D.; Buchmann, N. The match and mismatch between photosynthesis and land surface phenology of deciduous forests. *Agric. For. Meteorol.* **2015**, *214–215*, 25–38. [CrossRef]

87. Moura, Y.M.; Galvão, L.S.; dos Santos, J.R.; Roberts, D.A.; Breunig, F.M. Use of MISR/Terra data to study intra- and inter-annual EVI variations in the dry season of tropical forest. *Remote Sens. Environ.* **2012**, *127*, 260–270. [CrossRef]

88. Dong, J.; Xiao, X.; Wagle, P.; Zhang, G.; Zhou, Y.; Jin, C.; Torn, M.S.; Meyers, T.P.; Suyker, A.E.; Wang, J.; et al. Comparison of four EVI-based models for estimating gross primary production of maize and soybean croplands and tallgrass prairie under severe drought. *Remote Sens. Environ.* **2015**, *162*, 154–168. [CrossRef]

89. Sims, D.A.; Rahman, A.F.; Vermote, E.F.; Jiang, Z. Seasonal and inter-annual variation in view angle effects on MODIS vegetation indices at three forest sites. *Remote Sens. Environ.* **2011**, *115*, 3112–3120. [CrossRef]

90. Huete, A.R.; Didan, K.; Shimabukuro, Y.E.; Ratana, P.; Saleska, S.R.; Hutyra, L.R.; Yang, W.; Nemani, R.R.; Myneni, R. Amazon rainforests green-up with sunlight in dry season. *Geophys. Res. Lett.* **2006**, *33*. [CrossRef]

91. Babst, F.; Esper, J.; Parlow, E. Landsat TM/ETM+ and tree-ring based assessment of spatiotemporal patterns of the autumnal moth (*Epirrita autumnata*) in northernmost Fennoscandia. *Remote Sens. Environ.* **2010**, *114*, 637–646. [CrossRef]

92. Kharuk, V.I.; Ranson, K.J.; Im, S.T. Siberian silkmoth outbreak pattern analysis based on SPOT VEGETATION data. *Int. J. Remote Sens.* **2009**, *30*, 2377–2388. [CrossRef]

93. Lottering, R.; Mutanga, O. Optimising the spatial resolution of WorldView-2 pan-sharpened imagery for predicting levels of Gonipterus scutellatus defoliation in KwaZulu-Natal, South Africa. *ISPRS J. Photogramm. Remote Sens.* **2016**, *112*, 13–22. [CrossRef]

94. Eitel, J.U.H.; Vierling, L.A.; Litvak, M.E.; Long, D.S.; Schulthess, U.; Ager, A.A.; Krofcheck, D.J.; Stoscheck, L. Broadband, red-edge information from satellites improves early stress detection in a New Mexico conifer woodland. *Remote Sens. Environ.* **2011**, *115*, 3640–3646. [CrossRef]

95. Amaral, L.; Molin, J.P.; Portz, G.; Finazzi, F.B.; Cortinove, L. Comparison of crop canopy reflectance sensors used to identify sugarcane biomass and nitrogen status. *Precis. Agric.* **2014**, *16*, 15–28. [CrossRef]

96. Karande, B.I.; Lunagariya, M.M.; Patel, K.I.; Pandey, V. Model for Detecting Nitrogen Deficiency in Wheat Crop Using Spectral Indices. *J. Agrometeorol.* **2014**, *16*, 85–93. [CrossRef]

97. Groszyk, J.; Samborski, S.; Gozdowski, D.; Stępień, M.; Leszczyńska, E.; Rozbicki, J. Characterization of Winter Wheat Nitrogen Status with Vegetation Indices under Different Availability of Sulphur. In Proceedings of the Precision Agriculture 2015—Papers Presented at the 10th European Conference on Precision Agriculture, ECPA 2015, Volcani Center, Israel, 12–16 July 2015.

98. Modzelewska, A.; Stereńczak, K.; Mierczyk, M.; Maciuk, S.; Bałazy, R.; Zawiła-Niedźwiecki, T. Sensitivity of vegetation indices in relation to parameters of Norway spruce stands. *Folia For. Pol.* **2017**, *59*, 85–98. [CrossRef]

99. Ballester, C.; Hornbuckle, J.; Brinkhoff, J.; Smith, J.; Quayle, W. Assessment of In-Season Cotton Nitrogen Status and Lint Yield Prediction from Unmanned Aerial System Imagery. *Remote Sens.* **2017**, *9*, 1149. [CrossRef]

100. Handique, B.K.; Khan, A.Q.; Goswami, C.; Prashnani, M.; Gupta, C.; Raju, P.L.N. Crop Discrimination Using Multispectral Sensor Onboard Unmanned Aerial Vehicle. *Proc. Natl. Acad. Sci. India Sect. A Phys. Sci.* **2017**, *87*, 713–719. [CrossRef]

101. Cordero, E.; Moretti, B.; Miniotti, E.F.; Tenni, D.; Beltarre, G.; Romani, M.; Sacco, D. Fertilisation strategy and ground sensor measurements to optimise rice yield. *Eur. J. Agron.* **2018**, *99*, 177–185. [CrossRef]

102. Funk, C.C.; Brown, M.E. Intra-seasonal NDVI change projections in semi-arid Africa. *Remote Sens. Environ.* **2006**, *101*, 249–256. [CrossRef]

103. Weiss, J.L.; Gutzler, D.; Coonrod, J.E.A.; Dahm, C.N. Seasonal and inter-annual relationships between vegetation and climate in central New Mexico, USA. *J. Arid Environ.* **2004**, *57*, 507–534. [CrossRef]

104. Duarte, L.; Teodoro, A.C.; Gonçalves, H. Deriving phenological metrics from NDVI through an open source tool developed in QGIS. *Proc. SPIE* **2014**, *9245*, 924511. [CrossRef]

105. D'Arrigo, R.; Wilson, R.; Liepert, B.; Cherubini, P. On the 'Divergence Problem' in Northern Forests: A review of the tree-ring evidence and possible causes. *Glob. Planet. Chang.* **2008**, *60*, 289–305. [CrossRef]

106. Zhao, J.; Xiang, K.; Wu, Z.; Du, Z. Varying Responses of Vegetation Greenness to the Diurnal Warming across the Global. *Plants* **2022**, *11*, 2648. [CrossRef]

107. He, B.; Chen, A.; Jiang, W.; Chen, Z. The response of vegetation growth to shifts in trend of temperature in China. *J. Geogr. Sci.* **2017**, *27*, 801–816. [CrossRef]

108. Briffa, K.R.; Schweingruber, F.H.; Jones, P.D.; Osborn, T.J.; Shiyatov, S.G.; Vaganov, E.A. Reduced sensitivity of recent tree-growth to temperature at high northern latitudes. *Nature* **1998**, *391*, 678–682. [CrossRef]

109. Piao, S.; Nan, H.; Huntingford, C.; Ciais, P.; Friedlingstein, P.; Sitch, S.; Peng, S.; Ahlström, A.; Canadell, J.G.; Cong, N.; et al. Evidence for a weakening relationship between interannual temperature variability and northern vegetation activity. *Nat. Commun.* **2014**, *5*, 5018. [CrossRef]

110. Olsson, P.-O.; Lindström, J.; Eklundh, L. Near real-time monitoring of insect induced defoliation in subalpine birch forests with MODIS derived NDVI. *Remote Sens. Environ.* **2016**, *181*, 42–53. [CrossRef]

111. Townsend, P.A.; Singh, A.; Foster, J.R.; Rehberg, N.J.; Kingdon, C.C.; Eshleman, K.N.; Seagle, S.W. A general Landsat model to predict canopy defoliation in broadleaf deciduous forests. *Remote Sens. Environ.* **2012**, *119*, 255–265. [CrossRef]

112. Zhang, T.; Zhang, X.; Liu, H.; Pei, X. Application of Remote Sensing Technology in Monitoring Forest Diseases and Pests. *Plant Dis. Pests* **2010**, *1*, 57–62.

113. Datt, B. Remote Sensing of Chlorophyll a, Chlorophyll b, Chlorophyll a+b, and Total Carotenoid Content in Eucalyptus Leaves. *Remote Sens. Environ.* **1998**, *66*, 111–121. [CrossRef]

114. Gitelson, A.A.; Keydan, G.P.; Merzlyak, M.N. Three-band model for noninvasive estimation of chlorophyll, carotenoids, and anthocyanin contents in higher plant leaves. *Geophys. Res. Lett.* **2006**, *33*, L11402. [CrossRef]

115. Viña, A.; Gitelson, A.A.; Rundquist, D.C.; Keydan, G.; Leavitt, B.; Schepers, J. Monitoring Maize (*Zea mays* L.) Phenology with Remote Sensing. *Agron. J.* **2004**, *96*, 1139–1147. [CrossRef]

116. Wu, C.; Gonsamo, A.; Gough, C.M.; Chen, J.M.; Xu, S. Modeling growing season phenology in North American forests using seasonal mean vegetation indices from MODIS. *Remote Sens. Environ.* **2014**, *147*, 79–88. [CrossRef]

117. Gonsamo, A.; Chen, J.M.; Price, D.T.; Kurz, W.; Wu, C. Land surface phenology from optical satellite measurement and CO2eddy covariance technique. *J. Geophys. Res. Biogeosci.* **2012**, *117*. [CrossRef]

118. Garrity, S.R.; Bohrer, G.; Maurer, K.D.; Mueller, K.L.; Vogel, C.S.; Curtis, P.S. A comparison of multiple phenology data sources for estimating seasonal transitions in deciduous forest carbon exchange. *Agric. For. Meteorol.* **2011**, *151*, 1741–1752. [CrossRef]

119. Hall, R.; Castilla, G.; White, J.; Cooke, B.; Skakun, R. Remote sensing of forest pest damage: A review and lessons learned from a Canadian perspective. *Can. Èntomol.* **2016**, *148*, S296–S356. [CrossRef]

120. Coops, N.; Stanford, M.; Old, K.; Dudzinski, M.; Culvenor, D.; Stone, C. Assessment of Dothistroma Needle Blight of *Pinus radiata* Using Airborne Hyperspectral Imagery. *Phytopathology* **2003**, *93*, 1524–1532. [CrossRef]

121. Santos, M.J.; Greenberg, J.A.; Ustin, S.L. Using hyperspectral remote sensing to detect and quantify southeastern pine senescence effects in red-cockaded woodpecker (*Picoides borealis*) habitat. *Remote Sens. Environ.* **2010**, *114*, 1242–1250. [CrossRef]

122. Vrieling, A.; Skidmore, A.K.; Wang, T.; Meroni, M.; Ens, B.J.; Oosterbeek, K.; O'Connor, B.; Darvishzadeh, R.; Heurich, M.; Shepherd, A.; et al. Spatially detailed retrievals of spring phenology from single-season high-resolution image time series. *Int. J. Appl. Earth Obs. Geoinformation* **2017**, *59*, 19–30. [CrossRef]

123. Ciesla, W.M. European Woodwasp—A Potential Threat to North America's Conifer Forests. *J. For.* **2003**, *101*, 18–23.

124. Wulder, M.A.; Hilker, T.; White, J.C.; Coops, N.C.; Masek, J.G.; Pflugmacher, D.; Crevier, Y. Virtual constellations for global terrestrial monitoring. *Remote Sens. Environ.* **2015**, *170*, 62–76. [CrossRef]

125. Zhang, X.; Goldberg, M.D.; Yu, Y. Prototype for monitoring and forecasting fall foliage coloration in real time from satellite data. *Agric. For. Meteorol.* **2012**, *158–159*, 21–29. [CrossRef]